HYSTERESIS IN METHYLAMMONIUM LEAD IODIDE PEROVSKITE SOLAR CELLS: THE EFFECT OF CHANGING ELECTRON TRANSPORT LAYERS ON OBSERVED HYSTERESIS

A Thesis Submitted to the College of

Graduate and Postdoctoral Studies

In Partial Fulfillment of the Requirements

For the Degree of Master of Science

In the Department of Physics & Engineering Physics

University of Saskatchewan

Saskatoon

By

William Elcock

PERMISSION TO USE

In presenting this thesis/dissertation in partial fulfillment of the requirements for a Postgraduate degree from the University of Saskatchewan, I agree that the Libraries of this University may make it freely available for inspection. I further agree that permission for copying of this thesis/dissertation in any manner, in whole or in part, for scholarly purposes may be granted by Dr. Gap Soo Chang or, in their absence, by the Head of the Department or the Dean of the College in which my thesis work was done. It is understood that any copying or publication or use of this thesis/dissertation or parts thereof for financial gain shall not be allowed without my written permission. It is also understood that due recognition shall be given to me and to the University of Saskatchewan in any scholarly use which may be made of any material in my thesis.

Requests for permission to copy or to make other uses of materials in this thesis/dissertation in whole or part should be addressed to:

Head of the Department of Physics and Engineering Physics

53 Physics Building

116 Science Place

University of Saskatchewan

Saskatoon, Saskatchewan

S7N 5E2

Canada

OR

Dean

College of Graduate and Postdoctoral Studies

University of Saskatchewan

116 Thorvaldson Building, 110 Science Place

Saskatoon, Saskatchewan S7N 5C9

Canada

ABSTRACT

Perovskite solar cells (PSCs) have developed to the point where, currently, power conversion efficiencies (PCEs) in excess of 20% have been reported. This in contrast to the first PSC which was reported in 2009 with an efficiency of 3.8 %. This increase in PCE has helped to position PSCs as a photovoltaic technology which could potentially be commercialized. However, hysteretic current-density – voltage (J-V) behaviour has posed a challenge in the development of PSCs. When determining the efficiency of a PSC, their J-V characteristics are measured. However, their J-V response is sensitive to the voltage scan direction used when carrying out J-V tests. During these tests, measurement starts at 0V and ends at a suitable positive value. The direction in which the voltage was initially applied is then reversed during a second voltage scan. The resulting PCEs from each scan differs. This calls into question which value should be taken as correct. This variation in J-V response could also pose power quality issues when used in real world situations.

This work explores the origins of hysteresis in PSCs which use Titanium Dioxide (TiO_2) as an electron transport layer (ETL) and PSCs which use [6,6]-Phenyl C61 butyric acid methyl ester (PCBM). Devices illustrated in this work which were fabricated with a compact TiO_2 ETL, demonstrated more pronounced hysteresis when compared to devices which were fabricated using a mesoporous TiO_2 ETL. Hysteresis was minimal in the PSC which made use of the PCBM ETL.

This difference in hysteretic behaviour is attributed to differences in the built-in electric fields present in devices using compact, and/or mesoporous TiO_2 as an ETL.

ACKNOWLEDGEMENTS

I would like to thank the Organization of American States as well as the Latin American Scholarship Program of American Universities without whom this work would not have been possible. I also express my gratitude to my academic supervisor at the University of Saskatchewan, Professor Gap Soo Chang, who provided the necessary research support to complete this work. His feedback was invaluable in the process. The guidance of my committee members, Professors Michael Bradley, Sasha Koustov and Jean-Pierre St.-Maurice is also duly noted.

Thanks are extended to fellow group member Robert Bauer whose knowledge on the fabrication of organic solar cells was quite helpful in carrying out my research. In addition, Jesse Gordon, a 2017 summer student in the Chang group, was instrumental in assisting me with fabricating the final batches of solar cells I needed to complete my research. It would be remiss of me to not acknowledge his efforts. A special mention also goes out to Fatimah Almehmadi, also a group member.

Professor Timothy Kelly, of the Department of Chemistry at the University of Saskatchewan, along with his students Soumya Kundu, Philip Boutin and Kyle Fransishyn must be thanked for the knowledge they shared with me on the fabrication of perovskite solar cells. Professor Kelly's knowledge on the subject of perovskite solar cells is extensive and I thank him for sharing some of his wealth of knowledge with me. I also express gratitude to him for allowing me to utilize his laboratory space when it was necessary.

I also acknowledge Scott Noble of the Department of Mechanical Engineering at the University of Saskatchewan, who allowed me to use the ultraviolet and visible spectrophotometer in his laboratory to measure the absorption characteristics of my devices. He also aided me in the analysis of the data obtained.

Many thanks are extended to Debbie Gjertsen and Marjorie Granrude of the Department of Physics and Engineering Physics at the University of Saskatchewan for their assistance in all things administrative. Their extensive knowledge and experience was invaluable throughout the course of this work. Finally, my sincerest thanks go out to my family and friends, who supported me throughout my research process

DEDICATION

Dedicated to Wesley and Pamelia.

TABLE OF CONTENTS

LIST OF TABLES

LIST OF FIGURES

LIST OF ABBREVIATIONS

AM	Air Mass
CBM	Conduction band minimum
CH_3NH_3I	Methylammonium Iodide
$CH_3NH_3PbI_3$	Methylammonium Lead Iodide
CO_2	Carbon Dioxide
cp	Compact
DMF	N,N-Dimethylformamide
EHP	Electron-hole pair
FF	Fill factor
GIXRD	Grazing Incidence X-ray Diffraction
HOMO	Highest Occupied Molecular Orbital
I-V	Current-Voltage
J-V	Current-Density-Voltage
J_{MPP}	Maximum power point current-density
Li-TFSI	Li- bis(trifluoromethanesulfonyl)imide
LUMO	Lowest Unoccupied Molecular Orbital
L_e	Electron diffusion length
L_h	Hole diffusion length
MAI	Methylammonium Iodide
mp	Mesoporous
PCBM	[6,6]-Phenyl C_{61} butyric acid methyl ester
PEDOT:PSS	Poly(3,4-ethylenedioxythiophene)-poly(styrenesulfonate)
P3HT	Poly(3-hexylthiophene-2,5-diyl)

PbI_2	Lead Iodide
PCE	Power Conversion Efficiency
PSC	Perovskite Solar Cell
ITO	Indium Tin Oxide
SCL	Space Charge Layer
SMU	Source-Measure Unit
t-BP	4-tert-butyl- pyridine
TCO	Transparent Conducting Oxide
TiO_2	Titanium Dioxide
VBM	Valence band maximum
V_{MPP}	Maximum power point voltage
V_{OC}	Open-circuit Voltage

CHAPTER 1

INTRODUCTION

1.1 Background

The Intergovernmental Panel on Climate Change (IPCC) of the United Nations, which is made up of more than 1300 scientists, has predicted that global temperatures are likely to rise by about 2.5-10 ºC over the next century [1]. While this may seem inconsequential, temperature changes on the order of less than 10 ºC have been shown to correspond to significant environmental changes in the past [1]. When comparing temperature records from the beginning of the 20th century up until the present time to prior records, it can be seen that earth's average temperature has already increased by 1 ºC. Taking this into consideration, along with the predictions from the IPCC, it should also be noted that during the last ice age, the average temperature on earth was 5-9 ºC less than today's average temperature [1]. This period was marked by a level of ice coverage such that sea levels were around 120 to 135 m less than today's levels [2]. Bearing this in mind, it is reasonable to assume that increasing temperatures would affect the environment adversely as well.

Some of the predicted negative consequences of climate change in the future include more severe climate related events, such as increased periods of drought, more wildfires, and longer lasting, more intense tropical storms. In fact, global climate change has had effects on the environment already. These effects have manifested in the form of shrinking glaciers and other bodies of ice, as well as changes in the behaviour of animals and patterns of plant growth [1].

1.1.1 Proposed cause of climate change

The question now arises as to what has caused the observed temperature increase and corresponding negative effects. To address this question, one should take into consideration that the majority scientific consensus is that the increased average temperatures observed on earth is due to human activity [3]. One might now pose the question of how humans have brought about these changes. There are gases present in the earth's atmosphere which are responsible for the earth's warming climate. These include carbon dioxide, nitrous oxide and methane. While these gases are necessary for trapping heat from incoming solar radiation to maintain the earth at a

habitable temperature, human activities have played a part in increasing the amount of these gases in the earth's atmosphere to the point where the average temperature has increased.

One of the major contributors to the increased temperature is carbon dioxide (CO_2). Human activities have increased the levels of carbon dioxide present in the atmosphere. Burning of fossil fuels is one such activity. Fossil fuels are burned to provide energy for several reasons, including transportation and the production of electricity. The burning of fossil fuels is one of the major sources of anthropogenic, atmospheric CO_2. These fuels are carbon rich. When they are burned, carbon is combined with oxygen in the atmosphere, producing carbon dioxide.

1.2 Moving Forward: Perovskite Solar Cells

Continued burning of fossil fuels over the years has increased atmospheric CO_2 levels to the point where the heat trapping characteristics of the gas have helped contribute to the increased average temperature on earth. What can humanity do about this situation? As stated previously, the average temperature on the planet is expected to continue to rise. Instead of continuing to use fossil fuels as a primary energy source, alternative sources of energy which do not produce, or produce very little, greenhouse gases, should be explored. Photovoltaic (PV) solar cells are a viable option for providing at least some of the world's energy. Solar cells convert sunlight directly into electricity. This means that their performance is dependent on the amount of solar irradiation reaching them.

The most widespread types of solar cells are those based on crystalline and polycrystalline silicon wafers [4]. In order to produce these wafers, temperatures around 2000 $^{\circ}$C are required [5]. This high temperature results in a process which is costly overall. The associated costs limit the widespread implementation of crystalline, silicon-based solar cells. Perovskite solar cells (PSCs) are a hybrid organic/inorganic solar cell technology which can be manufactured via solution processes. This is advantageous because the solution processes used in the fabrication of PSCs are typically carried out at less than 500 ^{o}C and the small volume of solutions needed to produce PSCs [4,6]. Since PSCs can be produced using low temperature and therefore energy efficient processes, they could potentially be manufactured quite affordably. PSCs are therefore well positioned to contribute to the energy demands of the world with minimal greenhouse gas emissions. In addition, PSCs have been shown to exhibit power conversion efficiencies (PCEs) in excess of 20 % [7–9]. This could perhaps be viewed as impressive, considering that the PCE of the first PSC reported by

Miyasaka *et al*. in 2009 was just 3.8 % [10]. The most common type of PSC studied in research laboratories is based on methylammonium lead iodide ($CH_3NH_3PbI_3$).

1.3. Research Motivation: Hysteresis in Methylammonium Lead Iodide Perovskite Solar Cells

Despite high PCEs, the development and commercialization of perovskite-based solar cells have suffered from hysteretic current density-voltage (J-V) behaviours. Hysteresis in $CH_3NH_3PbI_3$ PSCs is characterized by a discrepancy between the J-V curves used to gauge their performance. A J-V curve illustrates the current response of a solar cell to a variety of voltages. The information used to create a J-V curve is ultimately used to calculate the PCE of a solar cell. A J-V curve is illustrated in Figure 1.1.

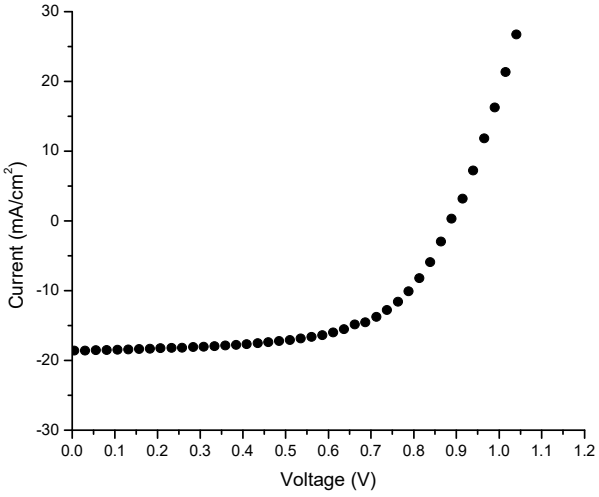

Figure 1.1. A J-V curve of a solar cell illustrating the current response to a series of applied voltages.

When characterizing a solar cell, the current response is measured over a series of voltages which are applied in a stepwise manner, from 0 to some forward bias voltage. These voltages are then applied in the reverse direction. With a $CH_3NH_3PbI_3$-based PSC, the J-V curves seldom correspond closely to each other. This is in contrast to other photovoltaic devices, such as silicon solar cells

and organic bulk heterojunction solar cells, whose J-V curves for either voltage scan direction are nearly identical. Hysteresis, as illustrated in Figure 1.2, makes it difficult to determine the efficiency of PSCs [11]. Moreover, this phenomenon would affect the output power quality of PSCs used in real world scenarios, due to the variation of current response when the size of the external load changes. The range of voltages applied during the recording of J-V curves is meant to simulate varied resistive loads [12]**.** It is evident from Figure 1.2, that depending on how the load attached to a PSC exhibiting hysteresis is varied, the current will not respond in an identical manner each time. This fluctuation in current output could damage electrical equipment. This work seeks to explore the mechanism of hysteresis in PSCs which make use of combinations of compact (cp) and mesoporous (mp) titanium dioxide. Gaining insight into J-V hysteresis in $CH_3NH_3PbI_3$ PSCs is an important step to finding effective solutions for minimizing its negative effects.

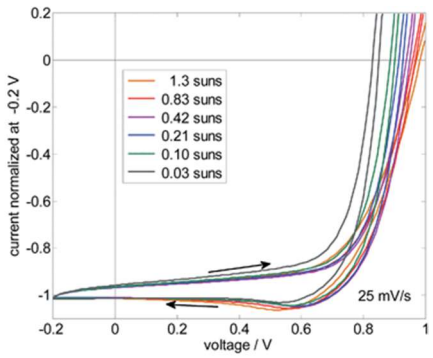

Figure 1.2. J-V curves of a PSC under illumination. The current response for a voltage application from 0V to around 1V (forward voltage scan) results in a different curve when compared to around 1 V to 0 V (reverse voltage scan) [11].

This work was undertaken with the following objectives:

- To investigate the hysteretic behaviour in PSCs
- To elucidate the influence of electron transport layer on the hysteretic behaviours in PSCs using cp-TiO_2, mp-TiO_2 and cp-TiO2/mp-TiO_2 as ETLs.
- Based on the proposed mechanism for hysteresis in cp-TiO_2, mp-TiO_2 and cp-TiO_2/mp-TiO_2 PSCs, suggest a PSC structure for improved hysteretic behaviour.
- To give a brief insight into possible avenues for future work related to the research highlighted here is also given.

CHAPTER 2

THEORY

2.1 Solar Cell Operation

The basic structure of $CH_3NH_3PbI_3$-based PSCs consists of a transparent front-contact electrode, an ETL, the $CH_3NH_3PbI_3$ active layer (perovskite layer), a hole transport layer (HTL) and a back-contact electrode as depicted in Figure 2.1. Note that in some inverted PSCs the positions of the HTL and ETLs are reversed.

Figure 2.1. A device structure of $CH_3NH_3PbI_3$-based PSC.

On absorbing photons of energy (E) larger than the bandgap energy (E_g), electrons are excited from the valence band of the $CH_3NH_3PbI_3$ active layer into the conduction band (CB) while leaving holes in the valence band (VB).

Since $CH_3NH_3PbI_3$ perovskite is a direct bandgap semiconductor, i.e., the valence band maximums and the conduction band minimums are aligned [13,14], direct excitation of an electron from the VB into the CB by a photon is allowed (see Figure 2.2).

After the generation of an electron-hole pair (EHP), the pair must be dissociated into a free electron and hole and transported to the solar cell's contact electrodes. For the $CH_3NH_3PbI_3$ PSCs investigated in this research, the contacts are indium tin oxide (ITO) and gold (Au). The mp-TiO_2, cp-TiO_2 and poly(3-hexylthiophene-2,5-diyl) (P3HT) layers, displayed in Figure 2.3 assist in the transport of charges to the contact electrodes.

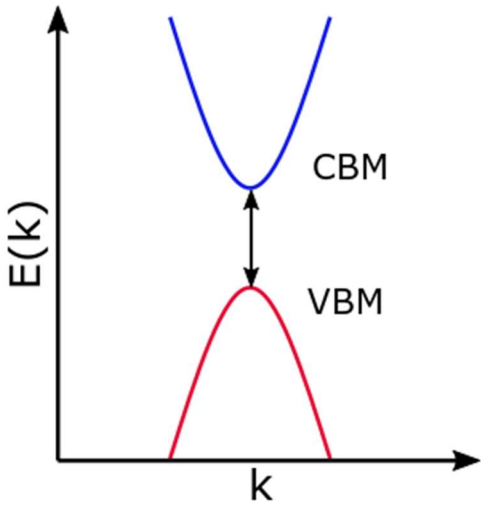

Figure 2.2: Direct bandgap excitation from the valence band maximum (VBM) to the conduction band minimum (CBM).

Figure 2.3 shows an energy-level diagram of a $CH_3NH_3PbI_3$-based PSC with TiO_2 and P3HT as ETL and HTL, respectively. The diagram illustrates how a photo-induced charge carrier (hole or electron) is transported in the $CH_3NH_3PbI_3$-based PSC. For ITO and Au electrodes, the relative positions of the Fermi levels (E_F) to vacuum level are displayed. Other materials are either hole selective or electron selective while $CH_3NH_3PbI_3$ is the semiconducting active material. The active layer is where charge carriers are generated. The VB maxima and CB minima of $CH_3NH_3PbI_3$ layer and TiO_2 are displayed with respect to vacuum level while the highest occupied molecular orbital (HOMO) and lowest unoccupied molecular orbital (LUMO) levels are indicated for a molecular material of P3HT. The energy level diagram gives a sense of how energetically favorable it is for charge carriers to travel through the VB or CB of a material. Generally, it is more energetically favorable for an electron to travel to a more negative energy level, while a hole prefers to travel to a more positive energy level. The ideal situation is to have HTLs and ETLs which accept their corresponding charge carriers but also block the opposite carrier. Figure 2.3 shows that electrons, generated in the $CH_3NH_3PbI_3$ can be transported to the TiO_2 layer, while holes are blocked since it is energetically unfavorable for holes to travel to the more negative VB level of TiO_2 from $CH_3NH_3PbI_3$. In addition, it is generally more energetically favorable for holes to be transported to more positive energy levels. Holes can therefore be easily transported to the

VB of P3HT, while at the same time, it is not energetically favorable for electrons to be transported to the CB of P3HT.

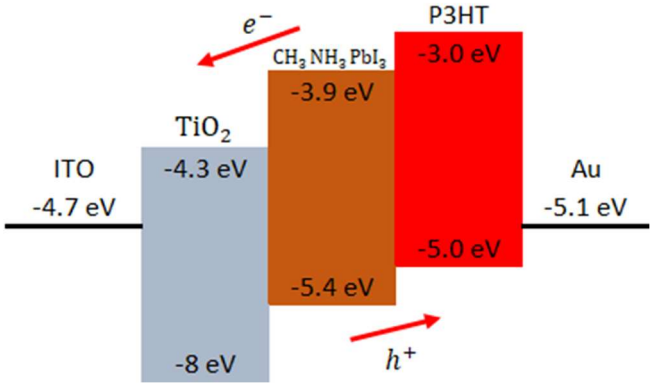

Figure 2.3. An energy-level diagram illustrating carrier transport in a $CH_3NH_3PbI_3$-based PSC with a TiO_2 ETL and a P3HT HTL.

To recap from above, the difference in the CB energy levels of the $CH_3NH_3PbI_3$ layer and the ETL ($E_{Per,CB}$-$E_{ETL,CB}$) drives electrons to the ETL where they are subsequently transported to the corresponding contact due to the difference between the CB of the ETL and the Fermi level of the contact ($E_{ETL,CB}$-E_{FA}). The difference between the VB of the $CH_3NH_3PbI_3$ layer and the VB of the HTL ($E_{Per,VB}$-$E_{HTL,VB}$) drives the transfer of holes from the $CH_3NH_3PbI_3$ layer to the HTL and the difference between the VB of the HTL and the fermi level of the corresponding contact ($E_{HTL,VB}$-E_{FB}) drives the transfer of holes from the HTL to this contact. However, it should be noted that these energy offsets are not the only conditions that need to be satisfied. The ionization potentials and electron affinities of the various layers must also be considered (Figure 2.4).

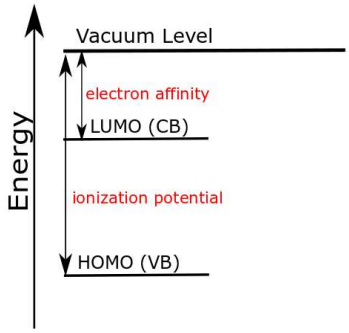

Figure 2.4. A representation of ionization potential an electron affinity with respect to HOMO (VB) and LUMO (CB) Levels.

The energy level diagram of the other PSC structure fabricated in this work is illustrated in Figure 2.5. This PSC makes use of an organic ETL in the form of [6,6]-Phenyl C_{61} butyric acid methyl ester (PCBM) and poly(3,4-ethylenedioxythiophene)-poly(styrenesulfonate) (PEDOT:PSS) as an HTL.

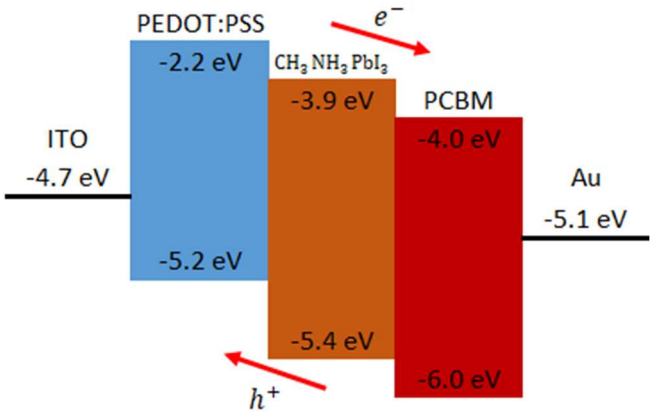

Figure 2.5. An energy level diagram illustrating carrier transport in a $CH_3NH_3PbI_3$-based PSC using a PCBM ETL and P3HT HTL.

Another factor that should be considered with $CH_3NH_3PbI_3$ PSCs is the thickness of the device. For a thin film solar cells, the diffusion length of charge carriers should also be considered. In other words, after an EHP is generated, electrons can only diffuse over a limited distance before recombining with a hole. However, in a $CH_3NH_3PbI_3$ PSC, the electron diffusion length (L_e) and hole diffusion length (L_h) are both in excess of 1 µm [15]. This means that the diffusion length is not a limiting factor in the PSCs fabricated in this work, since they are all less than 1 µm thick. Increasing thickness can also increase the series resistance (R_S) of a PSC and a balance must be found between maximizing on light absorption while decreasing R_S.

2.2 Solar Cell Behaviour

The ideal current density in a solar cell can be described by an equation as follows [16],

$$J = -J_{ph} + J_0 \left[e^{\frac{qV}{k_B T}} - 1 \right] \quad , \quad (2.1)$$

where J_{ph} is the photocurrent density, J_0 is a constant, V is the external bias voltage, k_B is Boltzmann's constant, q is the elementary charge, and T is the device temperature. This ideal solar cell can be modelled as in Figure 2.6 .

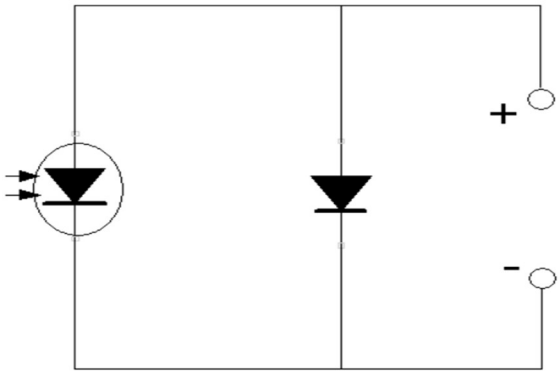

Figure 2.6. The equivalent circuit of an ideal solar cell.

The J-V curve of an ideal solar cell is similar to the plot illustrated in Figure 2.7.

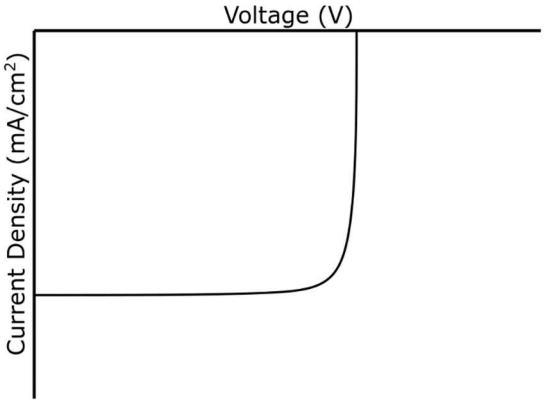

Figure 2.7. Representation of J-V curve of an ideal solar cell

Taking the influence of series and shunt resistances (R_S and R_{SH}, respectively) into consideration, the ideal solar cell equation is modified giving [13, 24],

$$J = -J_{ph} + J_0 \left[e^{\frac{q}{mk_BT}(V+JAR_S)} - 1 \right] - \frac{V + JAR_S}{AR_{SH}} \quad , \quad (2.2)$$

where m is the ideality factor and A is the cell area. Figure 2.7 can then be modified to Figure 2.8 which acts as a model for the solar cell which takes parasitic resistances into consideration.

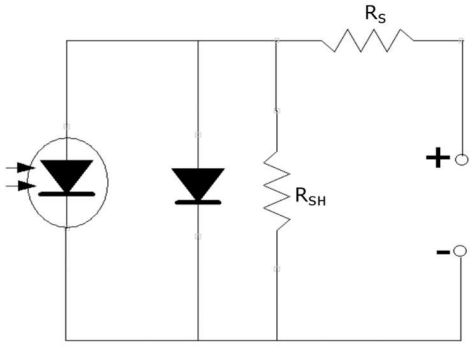

Figure 2.8. The equivalent circuit of a non-ideal solar cell with series and shunt resistances included.

Figure 2.9 illustrates the effect these parasitic resistances have on the J-V curves of solar cells. It is evident from Equation 2.2 that the higher the value of R_S, the lower the solar cell current. On the other hand, the lower the R_{SH}, the lower the solar cell current. Therefore, in an ideal scenario, the value of R_s should be as low as possible and R_{SH} as high as possible.

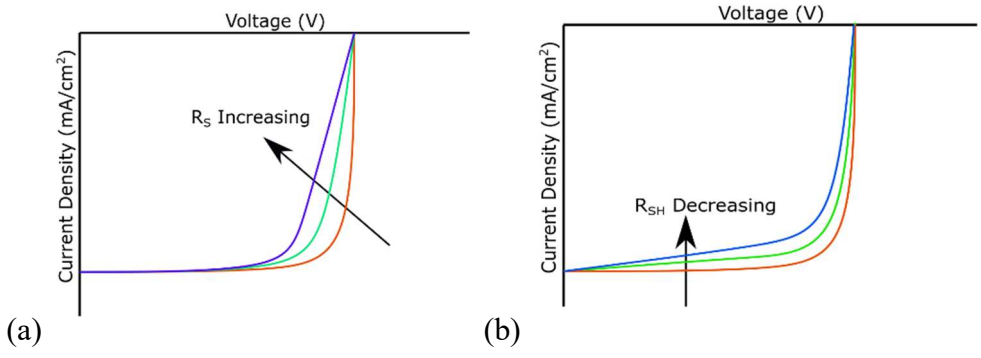

Figure 2.9. The effects of increasing R_S (a) and increasing R_{SH} (b) on the J-V curves of a solar cell.

Figure 2.10 can be used to model the performance of a non-ideal solar cell exhibiting hysteresis such as a $CH_3NH_3PbI_3$ PSCs [25, 26].

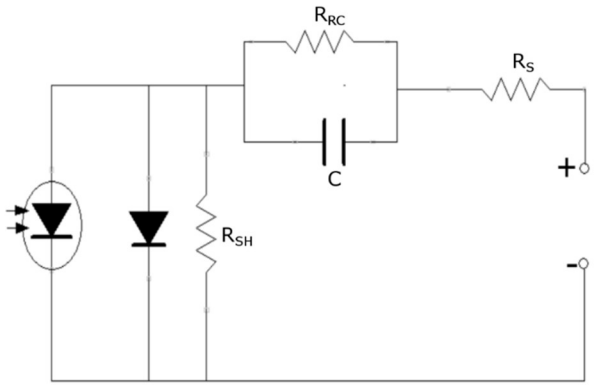

Figure 2.10. The equivalent circuit of a non-ideal solar cell with series and shunt resistances included. An R-C circuit is included which models the effect of hysteresis in $CH_3NH_3PbI_3$ PSCs.

The J-V curves which result due to such a solar cell are illustrated in Figure 2.11. The two J-V curves are obtained by the increasing bias from 0 V to positive voltage (forward scan) and then the decreasing bias back to 0 V (reverse scan). It is clearly seen that the reverse scan is different from the forward one and shows a higher PCE.

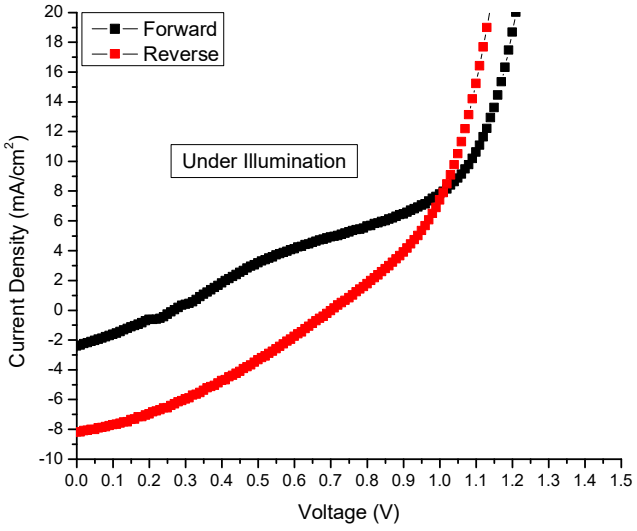

Figure 2.11. J-V curves of a solar cell displaying hysteretic J-V behaviour.

Now, taking the behaviour of $CH_3NH_3PbI_3$ PSCs into consideration, it is necessary to introduce some new variables. We will define the bias voltage as V_B and the voltage applied to an R-C circuit as V_{RC}. This gives,

$$V_{Tot} = V_B + V_{RC} + JAR_S \quad , \quad (2.3)$$

which leads to

$$J = -J_{ph} + J_0 \left[e^{\frac{qV_{Tot}}{mk_BT}} - 1 \right] - \frac{V_{Tot}}{R_{SH}} \quad . \quad (2.4)$$

2.3 Measurement of J-V Curves

2.3.1 Background

J-V curves provide useful information, related to the performance of a solar cell. One of the major pieces of information obtained is the power conversion efficiency (PCE). In order to obtain a J-V curve, the solar cell being tested is illuminated with a light source which closely matches the AM 1.5 solar spectrum and has a light intensity of 1000 W/m^2. In order for current to flow from the solar cell, a potential difference must be set up across the terminals. This usually happens in real world conditions when the solar cell is attached to a load. In a research environment, a current needs to flow in order to obtain the J-V curves. A series of J-V measurements are needed to get a useful result in the regime of 0 up to a positive voltage known as the open-circuit voltage (V_{OC}). The V_{OC} is the externally applied voltage that is needed to negate the built-in potential and flow of photo-induced carriers in a solar cell. At this point, the current density is zero. In a research environment, instead of using a variable resistive load which would more closely model what happens in real world operating conditions, it is more convenient to apply a series of external voltages across the solar cell's terminals, as this type of measurement can be taken quickly using a source-measure unit (SMU). The range of voltages is sourced and the corresponding current output from the solar cell is measured. These values are subsequently used to create J-V curves. An example of such a curve is illustrated in Figure 2.12 along with some relevant measurements.

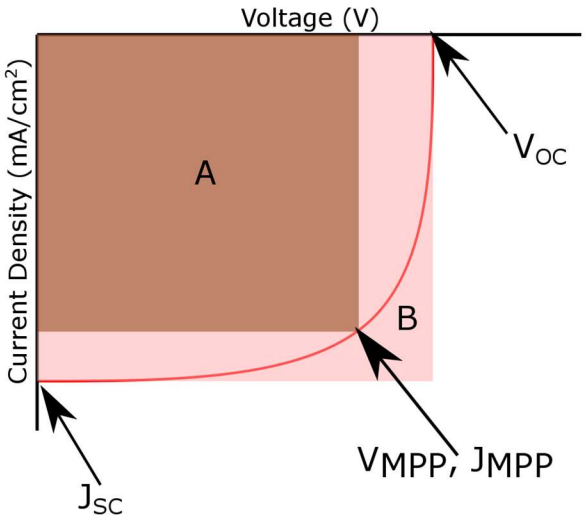

Figure 2.12. A J-V curve where the maximum power point voltage (V_{MPP}), the maximum power point current-density (J_{MPP}), J_{SC} and V_{OC} are indicated. For curves with the same values of J_{SC} and V_{OC}, area A will change depending on the values of V_{MPP} and J_{MPP}. This happens due to different values of R_S and R_{SH}.

In Figure 2.12, there are a number of parameters which are highlighted, however, based on the information provided by the curve, a quantity known as the fill factor (FF) can be calculated as shown below in Equation 2.5.

$$FF = \frac{Area\ A}{Area\ B} = \frac{J_{MPP}V_{MPP}}{J_{SC}V_{OC}} \tag{2.5}$$

The FF is directly affected by R_S and R_{SH}, which is evident from analyzing Figure 2.9. FF is often referred to as the "squareness" of a J-V curve [20]. The quantities outlined are determined by carrying out J-V measurements which ultimately allow for the calculation of the PCE which is given as,

$$PCE = \frac{J_{SC}V_{OC}FFA_{SC}}{P_{Sun}} = \frac{J_{MPP}V_{MPP}A_{SC}}{P_{Sun}} \tag{2.6}$$

where A_{sc} is the area of the solar cell and P_{Sun} is 1000 W/m^2.

2.3.2 Hysteresis Metric (þ)

In the results section, the level of hysteresis displayed by a PSC is quantified by displaying the difference in maximum power point (*MPP*) currents between the forward scan (curve obtained from scanning from 0 V to V_{OC}) and the reverse scan (curve obtained by scanning from V_{OC} to 0 V), by using the quantity ΔJ ($\Delta J = J_{MPP,Forward} - J_{MPP,Reverse}$), which is the difference between the current at the maximum power point (J_{MPP}) of the curve from 0 V to V_{OC} and the curve from V_{OC} to 0 V, as well as by using the metric

$$\text{þ} = \frac{J_{MPP,Forward}}{J_{MPP,Reverse}} \quad , \quad (2.7)$$

where $J_{MPP,Forward}$ is the value of J_{MPP} for the forward-scan curve, while $J_{MPP,Forward}$ is the value of J_{MPP} for the reverse-scan curve. ΔJ is illustrated in Figure 2.13.

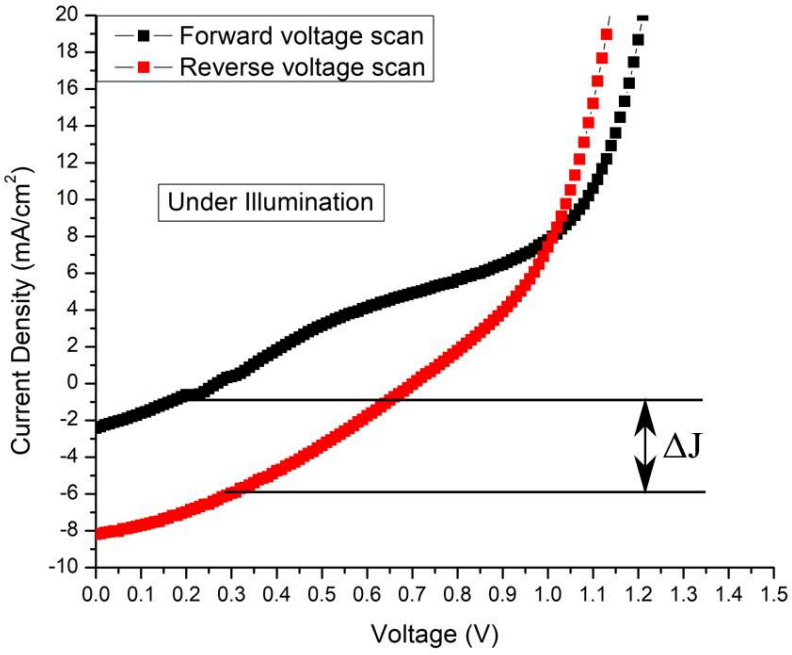

Figure 2.13. The J-V curves of a PSC exhibiting hysteretic J-V behaviour with ΔJ illustrated.

$CH_3NH_3PbI_3$ PSCs typically show higher PCEs for the reverse scan than for the forward scan [21]. Given that this is the case, higher values of *þ* indicate more stable power output.

2.4 Hysteresis Mechanism

$CH_3NH_3PbI_3$ PSCs which make use of titanium dioxide (TiO_2) ETLs, have been typically shown to exhibit hysteretic behaviours in the J-V curves [11,22]. However, it was also reported that this hysteresis can be reduced in devices making use of mesoporous mp -TiO_2 compared to those with a layer of cp-TiO_2 ETL [23–25]. Frolova *et al.* put forward that there is a photo-electrochemical reaction which occurs within the $CH_3NH_3PbI_3$ framework [26]. On exposure to light, they proposed that the following process occurs:

$$Pb^{+} + H^{+} \xrightarrow{hv} Pb^{2+} + H^{0} \quad . \quad (2.8)$$

Equation 2.8 results in negatively charged iodine vacancies and excess holes and thus explains the p-type behaviour of the $CH_3NH_3PbI_3$ [26]. The $CH_3NH_3PbI_3$ displays p-type character under exposure to light as explained in Chapter 4, and further by Frolova *et al.* [26]. Due to O_2 and Ti defects, TiO_2 displays n-type character. This results in a p-n junction being formed in the case of $CH_3NH_3PbI_3$ PSCs which make use of TiO_2 as an ETL. The p-n junction results in an electric field to which the drift and subsequent accumulation of I^- ions at the cp-TiO_2 (or ITO)/$CH_3NH_3PbI_3$ interface can be attributed to. These accumulated ions result in an electric field which acts against the transport of charge carriers from the $CH_3NH_3PbI_3$ layer to the ETL and HTL. To gain insight into why the PSC with cp-TiO_2 ETL displayed more severe hysteresis when compared to the PSCs with mp-TiO_2, it is necessary to examine the electric field which is brought about by the formation of a p-n junction.

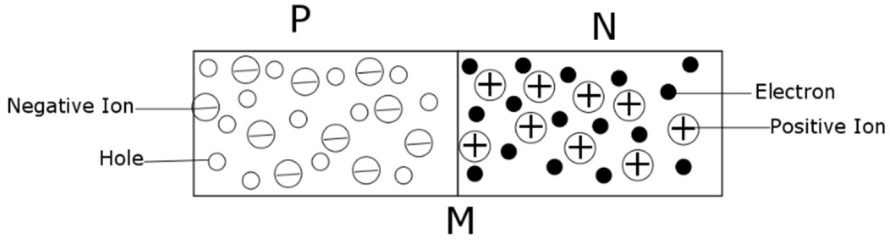

Figure 2.14. A simplified schematic of a p-n junction.

Figure 2.14 displays a simplified schematic of a p-n junction. The p-type side is labelled 'P', while the n-type side is labelled 'N'. The ionized donors, on the n-type side, and acceptors, on the p-type side are also displayed. In addition, the free electrons in the CB, on the n-type side are displayed, as well as the holes in the VB on the p-type side. We assume that there is a sharp discontinuity between the p-type and n-type regions. This is labelled 'M' in Figure 2.14 and is referred to as the metallurgical junction [16]. Since the p-type side possesses a greater concentration of holes than the n-type side, holes diffuse to the n-type side. Electrons are in greater concentration on the n-type side and subsequently diffuse toward the p-type side. However, these holes and electrons recombine near the junction at 'M'. This recombination leaves behind positive donor ions in the area near to 'M' on the n-type side and negative acceptor ions in the area near to M on the p-type side. This results in a charged region, referred to as the space charge layer (SCL) as indicated in Figure 2.15.

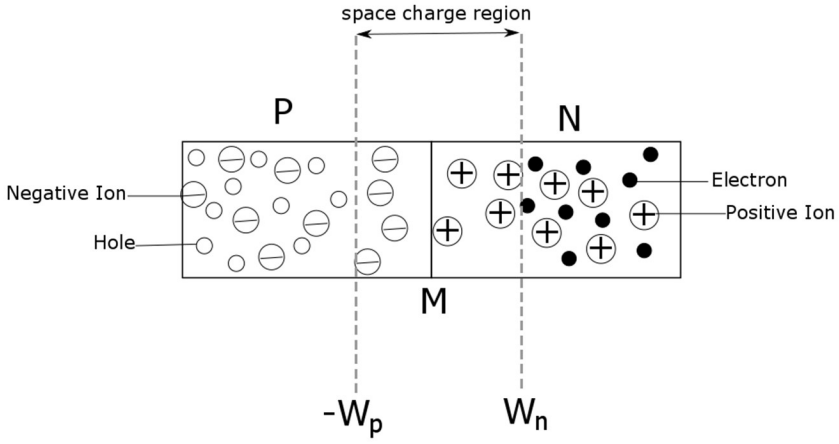

Figure 2.15. A simplified illustration of the space charge layer formed as a result of a p-n junction.

The space charge layer is also known as the depletion region [16]. There is an electric field, $E_{0,}$ built in due to the SCL and it points from the n-type side to the p-type side as illustrated in Figure 2.16. This field causes holes to drift back towards the p-type side and electrons towards the n-type side, acting in opposition to the diffusion that also occurs. In the dark, electrons and holes are drifted, increasing E_0 until an equilibrium is reached between the diffusion and drift forces. However, when the solar cell is illuminated, an EHP is generated and the electric field E_0 drifts,

electrons to the n-type side and holes to the p-type side. This results in the formerly neutral n-type side becoming negatively charged and the formerly neutral p-type side becoming positively charged. This sets up an open circuit voltage between the device terminals. Connection of the solar cell to an external circuit then results in a flow of electrons out of the device. These electrons do useful work before returning to the p-type side of the solar cell, recombining with the excess holes previously generated. This is what happens in the general case of a p-n junction where the ions are not mobile. However, since there are mobile I^- ions in a PSC, this can result in these ions being drifted to the cp-TiO_2 (or ITO)/$CH_3NH_3PbI_3$ interface. This results in a counter-field, E_A, as illustrated in Figure 2.16.

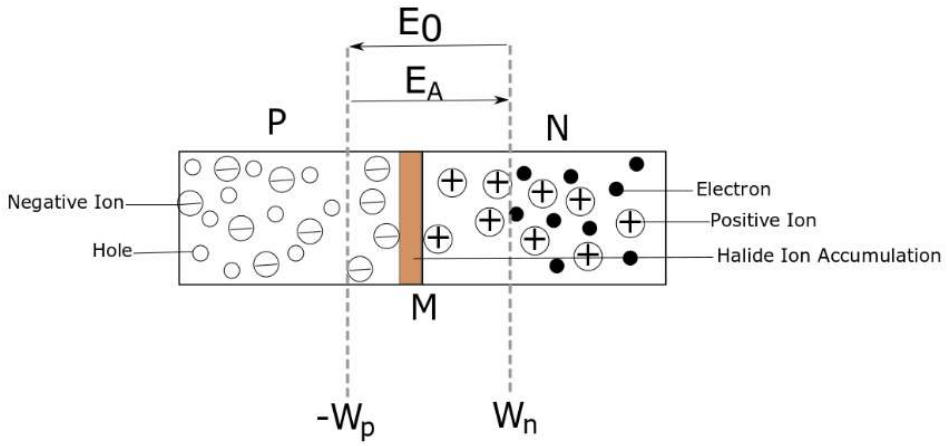

Figure 2.16. An illustration of the electric field set up as a result of the p-n junction, E_0, and the counter electric field E_A set up by the accumulation of I^- ions.

E_A acts in opposition to E_0 and in opposition to the flow of electrons to the n side of the PSC. When taking J-V measurements, the PSC is forward biased. As the bias is increased from 0 V to V_{OC} to measure the light up curve, E_A is strengthened by the external bias. This results in the reduced photovoltaic performance in the case of the light-up J-V curves, as compared to light down curves. When measuring the light down curves, voltage is scanned from V_{OC} to 0 V. This results in a reduction of the cumulative effect of the field due to the external bias and E_A as the external bias is decreased. In addition, the drift of I^- ions to the $CH_3NH_3PbI_3/TiO_2$ interface leads to accumulation. This means that eventually some of these ions will diffuse back to their original positions after a period of time. This is alluded to by Chen et al. [21] who highlighted the J-V

response of hysteretic $CH_3NH_3PbI_3$ PSCs. They observed that the current recorded at each voltage step of a J-V scan relaxes to a steady state current value after 5 s [25]. Even after 0.1 s, this relaxation process had already begun [21]. This relaxation to a steady state current value is illustrated in Figure 2.17. The $CH_3NH_3PbI_3$ PSCs fabricated in this work underwent J-V testing such that the voltage steps were in 0.1 V intervals and the dwell time at each voltage point was 10 ms. On switching to the reverse scan, it is expected that some of the ions will have already begun diffusion back to their original positions based on the observations of Chen et al. [21]. This means that E_A should be weaker at each voltage steps during the light-down scan than it was during the light-up scan. This ultimately results in a higher PCE for the light down J-V curve. On the surface, this may appear to indicate that the light-down curve only gives rise to a higher PCE when it is measured after the light up curve. However, this is not the case since the drift of I^- ions is activated by light. This means that even before an external bias is applied I^- ions will have already started drifting and the hysteretic behaviour outlined above should occur since E_A will always be strengthened during the light up J-V scan, regardless of if it is carried out first. It is apparent that J-V hysteretic behaviour is time dependent and Chen *et al.* have also highlighted the behaviour with J-V scans carried out very quickly (100, 000 mV/s) or very slowly (10 mV/s) will not display significant hysteresis. However, intermediate rates will result in hysteretic J-V curves. The mechanism behind the reduced hysteresis observed in $CH_3NH_3PbI_3$ PSCs is explored in the Results and Discussion section.

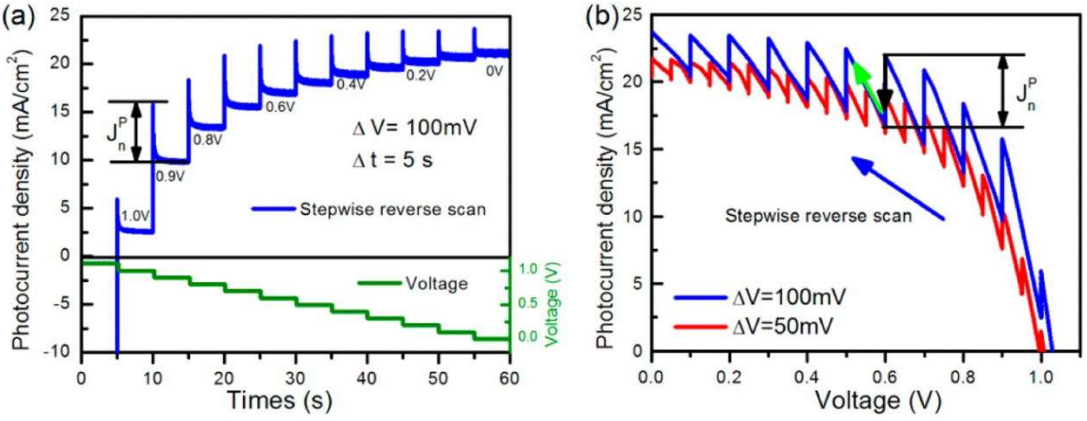

Figure 2.17. a) The time-dependent photocurrent response under stepwise reverse scan with 100 mV step size and 5 s step time [21]. b) J-V response under stepwise scan from 1.1 V to 0 V with 100 mV step size and step time of 5s [21]..

CHAPTER 3

SOLAR CELL DESIGN AND EXPERIMENTAL METHODS

3.1 Solar Cell Design

The basic structure of $CH_3NH_3PbI_3$ solar cells consists of a front contact, an electron transport layer (ETL), the $CH_3NH_3PbI_3$ active layer (perovskite layer), a hole transport layer (HTL) and a back contact. These layers are deposited on an ITO coated glass substrate. An illustration of this can be seen in Figure 3.1. From now on, the nomenclature of ITO/Transport Layer/$CH_3NH_3PbI_3$/Transport Layer/Au will be used to describe the PSC structures studied. This nomenclature lists layers starting from the ITO bottom layer and each item listed after every '/' is stacked on top of the previous layer. The structures studied in this work are ITO/compact titanium dioxide (cp-TiO_2)/mesoporous titanium dioxide (mp-TiO_2)/$CH_3NH_3PbI_3$/P3HT/Au, ITO/mp-TiO_2/$CH_3NH_3PbI_3$/P3HT, ITO/cp-TiO2/$CH_3NH_3PbI_3$/P3HT/Au and ITO/PEDOT:PSS/ $CH_3NH_3PbI_3$/PCBM/Au as displayed in Figure 3.1.

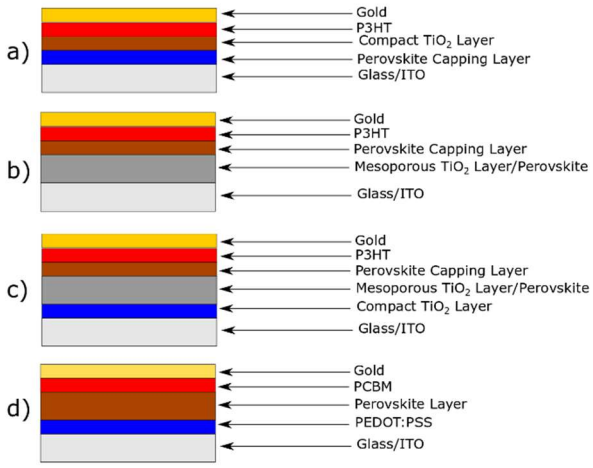

Figure 3.1 a) $CH_3NH_3PbI_3$ solar cell with a cp-TiO_2 ETL. b) $CH_3NH_3PbI_3$ PSC with a mp-TiO2 which acts as an ETL but also as a scaffold for the formation of the $CH_3NH_3PbI_3$ [29,30]. c) $CH_3NH_3PbI_3$ PSC with both cp-TiO_2 and mp-TiO_2 layers. d) $CH_3NH_3PbI_3$ PSC with a PEDOT:PSS HTL and PCBM ETL.

The substrates were acquired from Ossila® and are provided with the ITO pre-patterned onto the glass. The 6 ‘finger’ pattern pictured in Figure 3.2 allows for the fabrication of 6 different solar cells on one substrate. The contacts are necessary for the extraction of charge to the external circuit as well as for its return to the device.

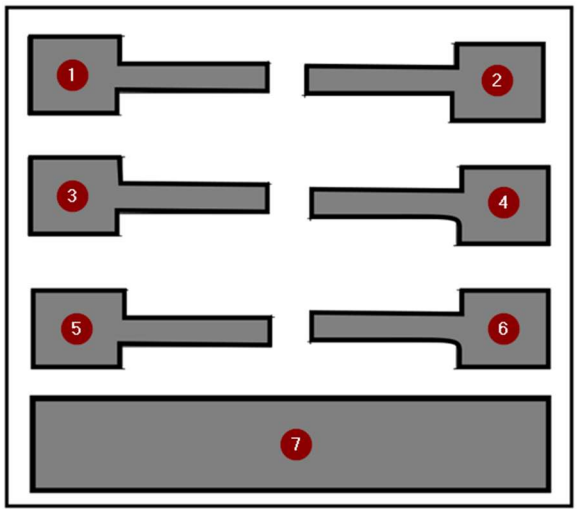

Figure 3.2. An Ossila® 6 pixel substrate. Item 1-6 are ITO ‘fingers’ which act as the anodes for 6 individual solar cells. These 6 solar cells share a common cathode strip which overlaps area 1-6 and makes contact with the ITO bar labelled as item 7. This allows for ease of attaching the probes used when taking J-V measurements.

The general fabrication procedure is illustrated in Figure 3.3. Image 1 shows a bare substrate. After a cleaning process, an ETL, an active layer, and a HTL are deposited using a spin-coating method, resulting in a coated area as represented in Image 2. The Au electrode is then deposited which is shown in Image 3. Next, the complete PSC is encapsulated to prevent the ingress of moisture and air (see Image 4). Finally, Image 5 represents connection legs attached to the ITO bars, to allow easy connection of the probes of the SMU when measuring J-V curves.

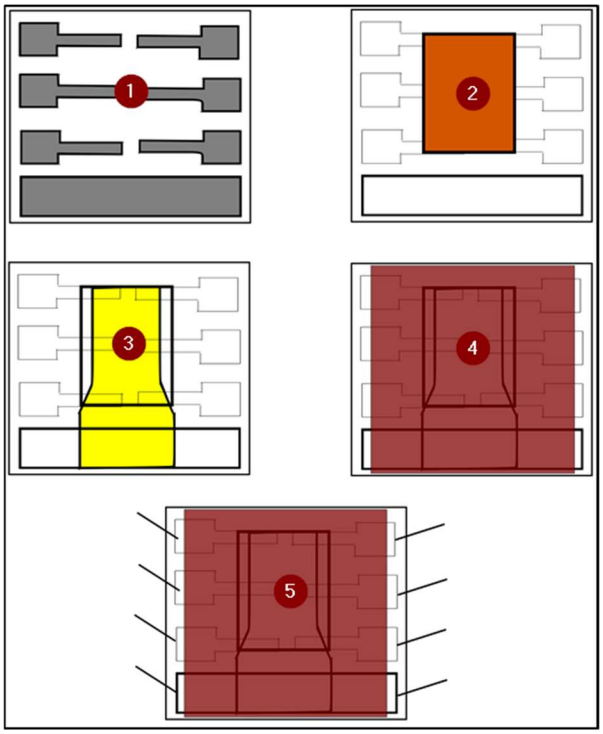

Figure 3.3. A general overview of the fabrication procedure of a $CH_3NH_3PbI_3$ PSC.

3.2 Materials

In order to get a better understanding of how a solar cell works, it is necessary to examine the materials it is made from. Each material performs different roles based on its properties.

3.2.1 Front Contact: ITO

The ITO is known as a transparent conducting oxide (TCO). It is an n-type semiconductor which exhibits a high level of degeneracy, which means that it has almost metallic conductivity (resistivity of about $2 \sim 4\times10^{-4}\ \Omega\cdot$cm) [27–29]. For this reason, it is widely used in a solar cell as a front contact. Due to its transparency, it allows light to enter the device while still performing its role as a contact.

3.2.2 Electron Transport Layer (ETL): TiO_2

The perovskite solar cells studied in this work use TiO_2 as an ETL. ETLs facilitate electron transport based on the energy position of their conduction bands, relative to the conduction band

of the active layer of the solar cell. As described in the previous chapter, it is more energetically beneficial for electrons to travel to a more negative energy level. This is again illustrated in Figure 3.4. For this reason, typically an ETL in a given solar cell configuration will posses a conduction band situated at a more negative than the active layer.

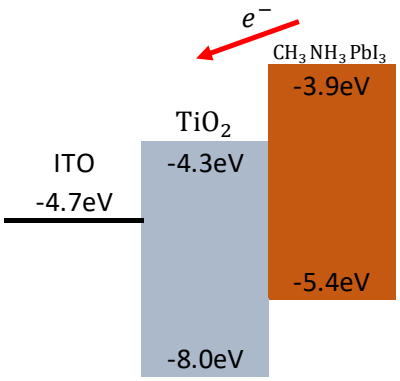

Figure 3.4. Electron transport from $CH_3NH_3PbI_3$ to TiO_2.

Due to oxygen (O) and titanium (Ti) defects within the TiO_2 crystal structure, there are mobile electrons not involved in bonding which cause TiO_2 to have an n-type character [30].

3.2.3 Electron Transport Layer (ETL): PCBM

As seen in Figure 3.5, PCBM is an organic, electron accepting material with high electron conductivity with an energy level which lends to favorable transport from $CH_3NH_3PbI_3$ [31].

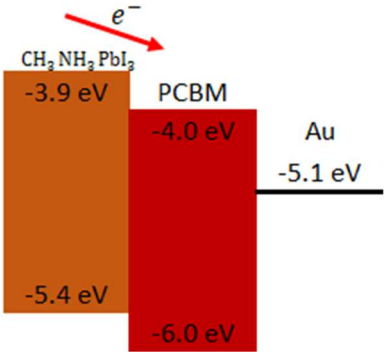

Figure 3.5. Electron transport from $CH_3NH_3PbI_3$ to PCBM.

3.2.4 Photoactive layer: $CH_3NH_3PbI_3$

$CH_3NH_3PbI_3$, pictured in Figure 3.6, is referred to as a perovskite due to it's chemical formula of the form ABX_3, where A (Pb^{2+}) and B ($CH_3NH_3^+$) are cations, where X (I^-) is an anion [32–34]. It is made by the combination of methylammonium iodide (CH_3NH_3I) and lead iodide (PbI_2) which are in powder form at room temperature.

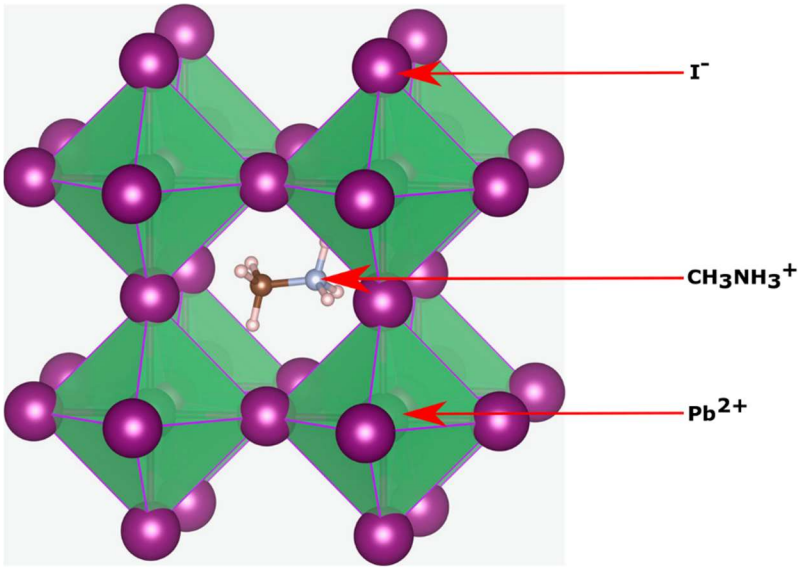

Figure 3.6. The structure of perovskite material, $CH_3NH_3PbI_3$. The molecule in the centre is a $CH_3NH_3^+$ ion. The purple spheres are I- ions which form octahedra at the centre of which are Pb^{2+} ions [35]. This image of the $CH_3NH_3PbI_3$ structure (https://www.nature.com/articles/ncomms8497) by Saiful *et al.* [35] is licensed under CC BY 4.0 (https://creativecommons.org/licenses/by/4.0/deed.en).

In the case of $CH_3NH_3PbI_3$, there is the $CH_3NH_3^+$ organic cation (A), the Pb^{2+} (B) metallic cation and the I^- organic anion (X). $CH_3NH_3PbI_3$ is a hybrid inorganic/organic semiconductor. It displays p-type character [36] which allows for the formation of p-n junctions with TiO_2[37]. Frolova *et al.* put forward that there is a photo-electrochemical reaction which occurs within the $CH_3NH_3PbI_3$ framework [26]. On exposure to light, they propose that the following occurs:

$$Pb^+ + H^+ \xrightarrow{hv} Pb^{2+} + H^0 \quad . \qquad (3.1)$$

Equation 3.1 results in negatively charged iodine vacancies and excess holes, resulting in p-type behaviour of the $CH_3NH_3PbI_3$ [26].

3.2.5 Hole Transport Layer (HTL): P3HT

P3HT is utilized as an HTL. HTLs facilitate hole transport based on the position of their valence bands, relative to the valence band of the active layer of the solar cell in question. As stated in the previous chapter, it is more energetically beneficial for holes to travel to a more positive energy level. This is illustrated in Figure 3.7. For this reason, typically an HTL in a given solar cell configuration will posses a valence band situated at a more positive energy level than the active layer.

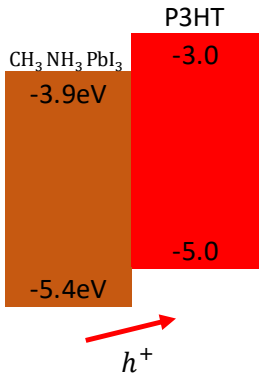

Figure 3.7. Hole transport from $CH_3NH_3PbI_3$ to P3HT.

The solutions of P3HT used in this work were mixed with Li- bis(trifluoromethanesulfonyl)imide (Li-TFSI) and 4-tert-butyl- pyridine (t-BP). Li-TFSI and t-BP increase the hole conductivity of P3HT [38].

3.2.6 Hole Transport Layer (HTL): PEDOT:PSS

PEDOT:PSS is an organic HTL with high conductivity. Its energy levels are such that it facilitates hole transport from $CH_3NH_3PbI_3$ to it as illustrated in Figure 3.8.

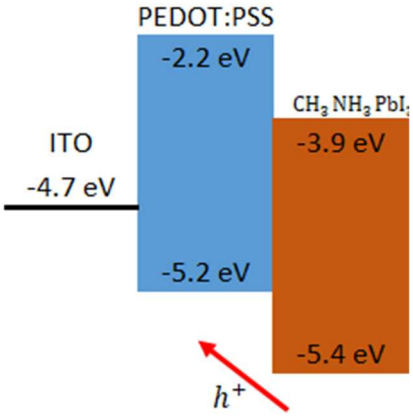

Figure 3.8. Hole transport from $CH_3NH_3PbI_3$ to PEDOT:PSS

3.3 Fabrication Methods

In order to deposit various layers of the $CH_3NH_3PbI_3$ solar cell, a combination of thin-film fabrication techniques are used. These are spin-coating, annealing and physical vapor deposition (PVD) via thermal evaporation. After all of the required layers are deposited, the solar cell is encapsulated to protect it against degradation due to exposure to moisture and air which can be detrimental to $CH_3NH_3PbI_3$ solar cells [39,40]. All spin-coating for this work was carried out in a N_2 filled glovebox (Figure 3.9) with a relative humidity controller installed. Humidity causes $CH_3NH_3PbI_3$ to degrade rapidly [39]. Humidity was always maintained below 10% during the fabrication process.

Figure 3.9. The N_2 filled glovebox used in this work.

3.3.1 Substrate Cleaning

Before PSCs were prepared, the Ossila® substrates were first thoroughly cleaned. The substrates were placed into a substrate holder which was then immersed into a beaker containing a hot solution of 10 % sodium hydroxide (NaOH) pellets dissolved in water. The beaker was placed into an ultrasonic cleaner and the substrates were sonicated for 10 minutes in order to remove any particulates, and organic materials. The substrates were then given 2 sequential baths of hot deionized water to rinse off the excess NaOH solution. Next, the substrates were sonicated in a hot bath of isopropanol and then given 2 additional rinses in hot baths of deionized water. Finally, the substrates were dried under a flow of dry N_2.

3.3.2 Spin-coating

Spin-coating is carried out to create uniform layers of thin films with thicknesses on the order of a few nm to a few μm [41]. For the PSCs in this work, spin-coating was used for the deposition of the cp-TiO_2 ETL, the mp-TiO_2 scaffold/ETL and the $CH_3NH_3PbI_3$ active layer. With spin-coating, a specified amount of solution of the material to be deposited is dropped onto a substrate while the substrate is rotating on the chuck of the spin-coater which contains a motor capable of high speed rotation. The substrate is held in position on the chuck by vacuum. Alternatively, some solutions are first dropped onto the substrate and then the substrate is made to rotate. In both cases, the rotation causes a centrifugal force which spreads the solution across the surface of the substrate. While spinning, the solvent evaporates, leaving behind a layer of the material in question. A simplified representation of the process can be viewed in Figure 3.10.

With spin-coating the thickness of the resulting film is proportional to the spin speed as follows:

$$t \propto \frac{1}{\sqrt{\omega}} \quad , \qquad (3.2)$$

where t is the thickness of the film and ω is the angular velocity.

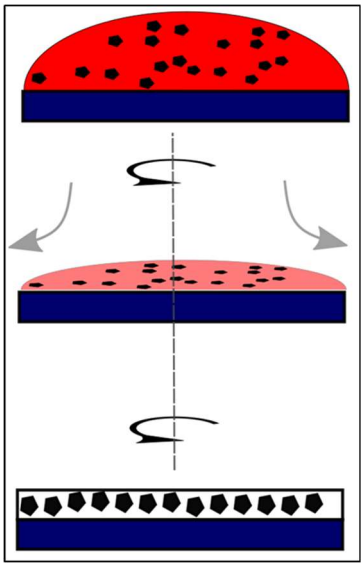

Figure 3.10. An illustration of the spin-coating process.

$$t \propto \frac{1}{\sqrt{\omega}}$$

3.3.3 Thermal Treatment

Annealing is necessary for the evaporation of residual solvent after spin-coating. It also promotes the self assembly of the precursor materials in solution [42,43]. Annealing is carried out by heating the substrate, with materials coated on top of it, at a predetermined temperature for a specified amount of time. The process is illustrated in Figure 3.11.

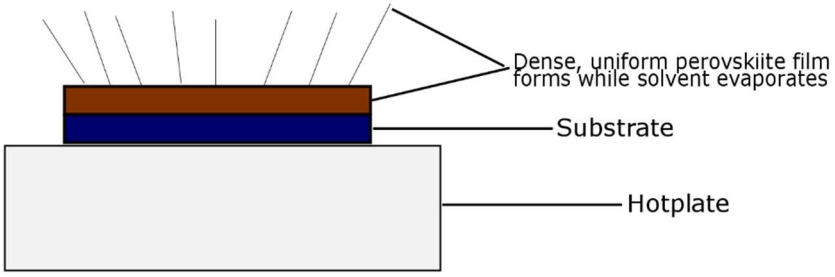

Figure 3.11. An illustration of solvent evaporating while a dense film of $CH_3NH_3PbI_3$ forms.

3.3.4 Thermal Evaporation Using a Physical Vapor Deposition Chamber

In this work, physical vapor deposition (PVD) through thermal evaporation was used for the deposition of the metal contact. Thermal evaporation was utilized in a vacuum chamber (Figure 3.12) at a pressure of approximately 10^{-7} torr. This allowed for the liberation of atoms from the surface of the Au pellets used. These atoms have a very low chance of interacting with extraneous gas particles due to the high vacuum [44]. With physical vapor deposition, the substrates are placed inside of a rotating substrate holder which controls the interaction of the substrates with the gas, allowing for a relatively uniform deposition of the desired material [45].

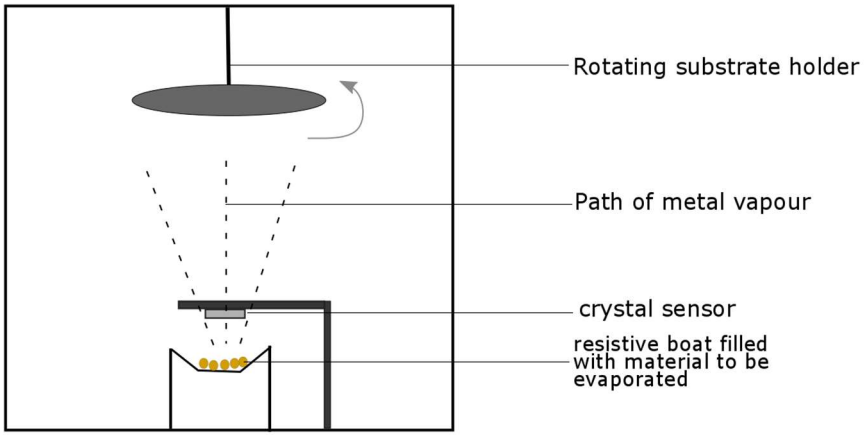

Figure 3.12. Schematic of physical vapor deposition chamber set up for thermal evaporation.

3.3.5 Encapsulation and attachment of connection legs

Encapsulation prevents the ingress of moisture and air into solar cells. In this work, after all of the requisite layers for the $CH_3NH_3PbI_3$ PSCs were deposited, a drop of Ossila® E131 UV curvrable epoxy which has been demonstrated to improve the lifetime of solar cells [46,47]. Figure 3.13 illustrates an encapsulated device with connection legs attached.

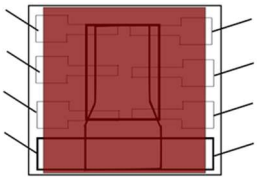

Figure 3.13. A completed, encapsulated solar cell, made on an Ossila® 6-pixel substrate. The colored area is covered in Ossila® E131 UV Curable epoxy and on top of that is a glass coverslip, preventing the ingress of moisture and air.

3.4 Fabrication Procedure

In this work, four types of complete PSCs were fabricated.The first 3 types made use of TiO_2 as an ETL. These were :

ITO/cp-TiO_2/$CH_3NH_3PbI_3$/P3HT/Au,

ITO/mp-TiO_2/$CH_3NH_3PbI_3$,

ITO/cp-TiO_2/mp-TiO_2/$CH_3NH_3PbI_3$/P3HT/Au

Finally a PSC of the structure ITO/PEDOT:PSS/$CH_3NH_3PbI_3$/PCBM/Au was also fabricated.

ITO/cp-TiO_2/$CH_3NH_3PbI_3$ and ITO/cp-TiO_2/mp-TiO_2/$CH_3NH_3PbI_3$ films were also prepared for cross-sectional scanning electron micrography(SEM). The different PSC structures were fabricated in order to probe the origin of reduced hysteresis in $CH_3NH_3PbI_3$ PSCs.

3.4.1 ITO/cp-TiO_2/$CH_3NH_3PbI_3$/P3HT/Au

The first step in fabricating devices with the structure ITO/cp-TiO_2/$CH_3NH_3PbI_3$/P3HT/Au was the deposition of the cp-TiO_2 layer. This was achieved using a technique demonstrated by Lee *et al.* [48]. The following steps were all carried out inside of a N_2 purged glovebox. First, a 0.1 Molar solution of Titanium diisopropoxide bis(acetylacetonate) in 1-butanol was spin-coated onto a substrate at 2000 rpm 3 times. Between each coating, the substrates were placed on a hotplate set to 125ºC for 5 minutes in order to dry the deposited layers. After the third spin-coating of the Titanium diisopropoxide bis(acetylacetonate) solution, the substrates were gradually heated to 450ºC and were left to sinter for 20 min. They were then allowed to cool to room temperature.

The next step was the deposition of the $CH_3NH_3PbI_3$ layer. This was done via a two-step spin coating method as demonstrated by Grätzel *et al.*[49]. First a 462 mg/ml solution of PbI_2 in N,N-Dimethylformamide (DMF) was spin coated on top of the cp-TiO_2 layer at 3000 rpmfor 5 seconds and then 6000 rpm for 5 seconds. The spin speed was switched 'on the fly' with no break between the switch. Next, the PbI_2 layer was allowed to dry on the hotplate at 40 ^oC for 3 min and then 100 ^oC for 5 min. The substrates were then allowed to cool down to room temperature. Subsequently a 6 mg/mL solution of methylammonium iodide (MAI) was spin-coated onto the PbI_2 layer of the substrates for 20 seconds at 4000 rpmThe substrates were then dried at 100 ^oC for 5 min which allowed the $CH_3NH_3PbI_3$ to form uniformly.

Afterward, a 10 mg/ml solution of P3HT with 3.4 µl of 4-tert-butylpyridine and 6.8 µl of a 28 mg/ml lithium–bis(tri-fluoromethanesulfonyl)imide (Li–TFSI) solution added, prepared according to the methods of Kelly *et al.* [50], was spin-coated on top of the other layer at 1000 rpm for 30 seconds.

Note that after the deposition of each layer, the cathode bar of the Ossila® substrates was wiped clean, in preparation for the deposition of the Au cathode. The cleaning step is done to prevent a short-circuit occurring. Without cleaning, the anodes of the 6-pixel substrate would be directly connected to the cathode bar, causing a short-circuit. The solvent which was used to create the solution that was spin-coated is also used to wipe the cathode bar clean.

Finally, the substrates were removed from the N_2 purged glovebox and placed inside of a cathode mask. They were then mounted onto the sample holder of the PVD system. Au pellets were loaded into the resistive heater of the PVD system. The sample holder was mounted inside of the PVD system chamber which was pumped down to a pressure of around 10^{-7} torr. The Au pellets were subsequently thermally evaporated while the substrates were spinning, until the deposition of 150 nm of Au was completed as measured by the crystal sensor, inside of the PVD system chamber. This was in accordance with a similar technique used by Grätzel *et al.*[49].The substrates with the various layers deposited on top were encapsulated in order to protect the completed solar cells from moisture and oxygen after the deposition of Au.

3.4.2 ITO/mp-TiO_2/$CH_3NH_3PbI_3$/P3HT/Au

The first step in fabricating devices with the structure ITO/cp-TiO_2/mp-TiO_2/$CH_3NH_3PbI_3$/P3HT/Au was the deposition of the cp-TiO_2 layer. To do this, a solution of Dyesol® 18-NRT TiO_2 paste, dissolved in ethanol in a 1:4 ratio by weight, was spin-coated onto a substrate at 6000 rpm. for 30 s. The substrates were then gradually heated to 500°C and left to sinter for 30 minutes. This was carried out in accordance with the methods of Bu *et al.*[51].

The next step was the deposition of the $CH_3NH_3PbI_3$ layer. This was done via a two-step spin-coating method as demonstrated by Grätzel *et al.*[49]. First, a 462 mg/ml solution of PbI_2 in N,N-Dimethylformamide (DMF) was spin coated on top of the cp-TiO_2 layer at 3000 rpm for 5 seconds and then 6000 rpm. for 5 seconds. The spin speed was switched 'on the fly' with no break between the switch. Next, the PbI_2 layer was allowed to dry on the hotplate at 40°C for 3 minutes and then 100°C for 5 minutes. The substrates were then allowed to cool down to room temperature. Subsequently a 6 mg/mL solution of MAI was spin-coated onto the PbI_2 layer of the substrates for 20 seconds at 4000 rpm The substrates were then dried at 100°C for 5 minutes which allowed the $CH_3NH_3PbI_3$ to form uniformly.

Afterward, a 10 mg/ml solution of P3HT with 3.4 µl of 4-tert-butylpyridine and 6.8 µl of a a 28 mg/ml lithium–bis(tri-fluoromethanesulfonyl)imide (Li–TFSI) solution added, prepared according to the methods of Kelly *et al.* [50] was spin-coated on top of the other layers at 1000 rpm for 30 s. Note that after the deposition of each layer, the cathode bar of the Ossila® substrates was wiped clean, in preparation for the deposition of the Au cathode deposition. The cleaning step is done to prevent a short-circuit occurring. Without cleaning, the anodes of the 6-pixel substrate would be directly connected to the cathode bar. The solvent which was used to create the solution that was spin-coated is also used to wipe the cathode bar clean.

Finally, the substrates were removed from the N_2 purged glovebox and placed inside of a cathode mask. They were then mounted onto the sample holder of the PVD system. Au pellets were loaded into the resistive heater of the PVD system. The sample holder was mounted inside of the PVD system chamber which was pumped down to a pressure of around 10^{-7} torr. The Au pellets were subsequently thermally evaporated while the substrates were spinning, until the deposition of 150 nm of Au was completed as measured by the crystal sensor, inside of the PVD system chamber. This was in accordance with a similar technique used by Grätzel *et al.* [49]. The substrates with

the various layers deposited on top were encapsulated in order to protect the completed solar cells from moisture and oxygen after the deposition of Au.

3.4.3 ITO/cp-TiO_2/mp-TiO_2/$CH_3NH_3PbI_3$/P3HT/Au

The first step in fabricating devices with the structure ITO/cp-TiO_2/mp-TiO_2/$CH_3NH_3PbI_3$/ P3HT/Au was the deposition of the cp-TiO_2 layer which was achieved using a technique demonstrated by Lee *et al.* [48]. The following steps were carried out inside of a N_2 purged glovebox. Firstly, a 0.1 molar solution of titanium diisopropoxide bis(acetylacetonate) in 1-butanol was spin-coated onto a substrate at 2000 rpm 3 times. Between each coating, the substrates were placed on a hotplate set to 125 ºC for 5 minutes, in order to dry the deposited layers. After the third spin-coating of the titanium diisopropoxide bis(acetylacetonate) solution, the substrates were gradually heated to 450ºC and were left to sinter for 20 minutes. They were then allowed to cool to room temperature.

After cooling, a solution of Dyesol® 18-NRT TiO_2 paste, dissolved in ethanol in a 1:4 ratio by weight, was spin-coated on top of the cp-TiO_2 layer at 6000 rpm for 30 s. The substrates were then gradually heated to 500ºC and left to sinter for 30 minutes. This was carried out in accordance with the methods of Bu *et al.* [51].

The next step was the deposition of the $CH_3NH_3PbI_3$ layer. This was done via a two-step spin coating method as demonstrated by Grätzel *et al.* [49]. First a 462 mg/ml solution of PbI_2 in N,N-Dimethylformamide (DMF) was spin coated on top of the cp-TiO_2 layer at 3000 rpm for 5 seconds and then 6000 rpm for 5 seconds. The spin speed was switched 'on the fly' with no break between the switch. Next, the PbI_2 layer was allowed to dry on the hotplate at 40 ºC for 3 minutes and then 100 ºC for 5 minutes. The substrates were then allowed to cool down to room temperature. Subsequently a 6 mg/ml solution of MAI was spin-coated onto the PbI_2 layer of the substrates for 20 seconds at 4000 rpm. The substrates were then dried at 100ºC for 5 minutes which allowed the $CH_3NH_3PbI_3$ to form uniformly.

Afterward, a 10 mg/ml solution of P3HT with 3.4µl of 4-tert-butylpyridine and 6.8µl of a 28mg/ml lithium–bis(tri-fluoromethanesulfonyl)imide (Li–TFSI) solution added, prepared according to the methods of Kelly *et al.* [50] was spin-coated on top of the other layers at 1000 rpm for 30 seconds.

Note that after the deposition of each layer, the cathode bar of the Ossila® substrates was wiped clean, in preparation for the deposition of the Au cathode. The cleaning step is done to prevent a short-circuit occurring since without cleaning, the anodes of the 6-pixel substrate would be directly connected to the cathode bar. The solvent which was used to create the solution that was spin-coated is also used to wipe the cathode bar clean.

Finally, the substrates were removed from the N_2 purged glovebox and placed inside of a cathode mask. They were then mounted onto the sample holder of the PVD system. Au pellets were loaded into the resistive heater of the PVD system. The sample holder was mounted inside of the PVD system chamber which was pumped down to a pressure of around 10^{-7} torr. The Au pellets were subsequently thermally evaporated while the substrates were spinning, until the deposition of 150 nm of Au was completed as measured by the crystal sensor, inside of the PVD system chamber. This was in accordance with a similar technique used by Grätzel *et al.* [49]. The substrates with the various layers deposited on top were encapsulated in order to protect the completed solar cells from moisture and oxygen after the deposition of Au.

3.4.4 ITO/PEDOT:PSS/$CH_3NH_3PbI_3$/PCBM/Au Solar Cells

The first step in fabricating this PSC structure was the spin-coating of PEDOT:PSS onto an Ossila® substrate at 3000 rpm for 1 minute. After this step was completed, the substrates were dried on a hotplate at around 150 $^{\circ}$C for a period of 5 min.

Next, the first step in forming the $CH_3NH_3PbI_3$ layer was executed according to the methods of Grätzel *et al.* [52]. First a 462 mg/mL solution of PbI_2 in N,N-Dimethylformamide (DMF) was spin coated on top of the cp-TiO_2 layer at 3000 rpm for 5 seconds and then 6000 r for 5 seconds. The spin speed was switched 'on the fly' with no break between the switch. Next, the PbI_2 layer was allowed to dry on the hotplate at 40^{o} C for 3 min and then 100^{o} C for 5 min. The substrates were then allowed to cool down to room temperature. Subsequently a 6 mg/ml solution of Methylammonium Iodide was spin-coated onto the PbI_2 layer of the substrates for 20 seconds at 4000 rpm. The substrates were then dried at 100^{o} C for 5 min which allowed the $CH_3NH_3PbI_3$ to form uniformly.

Following the formation of the $CH_3NH_3PbI_3$ layer, a layer of PCBM was deposited. This was done by spin-coating a 20 mg/ml solution of PCBM dissolved in chlorobenzene onto the substrate according to the methods of Heo *et al.* [53].

Note that after the deposition of each layer, the cathode bar of the Ossila® substrates was wiped clean, in preparation for the deposition of the Au cathode. The cleaning step is done to prevent a short-circuit occurring since without cleaning, the anodes of the 6-pixel substrate would be directly connected to the cathode bar. The solvent which was used to create the solution that was spin-coated is also used to wipe the cathode bar clean.

Finally, the substrates were removed from the N_2 purged glovebox and placed inside of a cathode mask. They were then mounted onto the sample holder of the PVD system. Au pellets were loaded into the resistive heater of the PVD system. The sample holder was mounted inside of the PVD system chamber which was pumped down to a pressure of around 10^{-7} torr. The Au pellets were subsequently thermally evaporated while the substrates were spinning, until the deposition of 150 nm of Au was completed as measured by the crystal sensor, inside of the PVD system chamber. This was in accordance with a similar technique used by Grätzel *et al.* [49]. The substrates with the various layers deposited on top were encapsulated in order to protect the completed solar cells from moisture and oxygen after the deposition of Au.

3.5 Characterization of $CH_3NH_3PbI_3$ Solar Cells

In order to characterize the device performance of the fabricated PSCs, the J-V curves were first measured and used to determine the PCEs . SEM images were also taken in order to gain further insight into the topology of the fabricated PSCs. Finally, UV-Vis spectroscopy was carried out in order to determine the light absorption characteristics of the PSCs.

3.5.1 J-V Curves and PCE Determination

J-V curves were taken using an OAI® solar simulator which consists of the following components:

- A 350W xenon arc lamp which provides illumination with the intensity of 1000 W/m^2 which is defined as 1 sun illumination.

- An AM 1.5 filter which causes the light emitted by the Xenon arc lamp to mimic the Am 1.5 spectrum
- A Keithley 2420 SMU which provides a series of source voltages to the solar cells being tested in forward bias, and subsequently measures the current. This data is used to create the J-V curves.

Before measuring the J-V curves of a solar cell, the Xenon arc lamp must be allowed to warm up first to ensure that the spectrum of light it emits is as consistent as possible. The intensity of the light is then verified using a Newport silicon reference cell (Figure 3.14). A reference cell is used to verify that the solar simulator is producing light of intensity 1000 W/m^2.

Figure 3.14. A Newport 91150V silicon reference cell.

In this work, each solar cell on a particular substrate was measured. An Ossila® active area mask is placed on top of the substrate in order to define 6 active areas of 0.0212 cm^2. Forward bias is achieved by attaching the negative lead of the Keithley 2420 to one of the 6 anode bars and the positive lead of the Keithley 2420 to the cathode bar of the substrate being analyzed and applying voltages in the range of 0 V to V_{OC}. All 6 solar cells on a substrate share the cathode, which means that positive lead of the SMU does not need to be moved during the series of 6 measurements that are needed. However, the negative lead must be attached to each anode's corresponding electrical connection leg in order to switch solar cells. The order of lead attachment is reversed in the PSC which makes use of PEDOT:PSS.

A series of voltages are applied from 0 to V_{OC}, in steps of 0.1 V, and the corresponding current values are recorded. Recording is done via a computer interface with the SMU. The OAI® solar simulator is pictured below in Figure 3.15.

Figure 3.15. The OAI solar simulator with built-in Keithley 2420 SMU used in this work.

3.5.2 Scanning Electron Micrography (SEM)

3.5.2.1 Background

A scanning electron microscope is used to provide high magnification images of a sample. Depending on he instrument, image magnification o0f 3x to 500 000 is possible [54]. This image is achieved by scanning a high energy, highly focused beam of electrons across the surface of a sample. When the high energy electrons make an impact with the sample, secondary electrons are emitted which are measured by a detector which allows for the generation of a real-time image. The emission of secondary electrons is strongly influenced by the surface topography of the sample being imaged [54]. For this reason, the emission of secondary electrons allows for analysis of the topography of a sample.

3.5.2.2 SEM Measurements

SEM images of films corresponding to the 2 device structures studied were taken in order using a Hitachi SU8010 cold field emission scanning electron microscope. In this work, cross-sectional SEM images were taken. However, this type of image is taken in the same manner as a surface SEM image. The sample being measured is merely cut and rotated in order to view the cross section.

3.5.3 Ultraviolet-Visible (UV-Vis) Spectroscopy

3.5.3.1 Background

Uv-Vis Spectroscopy is carried out using a UV-Vis spectrophotometer. A light source inside of the spectrophotometer is split into individual wavelengths of light in a section of the device called the monochromator. The resulting beam of light is then split into two. There are two cells which the light must pass through; the reference cell and the sample cell. After the light passes through each cell, the resulting intensity is measured using photodiode detectors. A reference material with known optical properties is mounted in the reference cell, while the sample to be measured is placed in the sample cell. The intensity recorded by the detector corresponding to the reference cell is used to calculate the absorbance of the sample in the sample cell, based on the intensity recorded by the sample cell's detector. This is shown in Equation 3.3,

$$abs = log \frac{I}{I_0} \quad , \quad (3.3)$$

where *abs* is the absorbance, *I* is the intensity recorded by the sample detector, and I_0 is the intensity recorded by the reference detector.

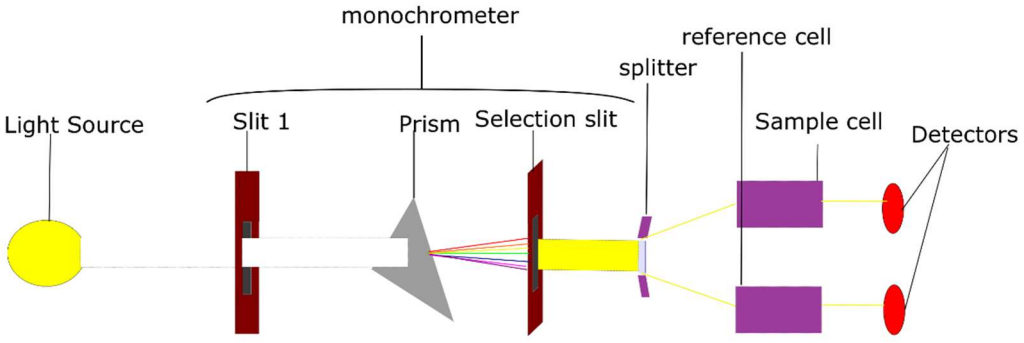

Figure 3.16. A simplified schematic of a UV-Vis spectrophotometer.

3.5.3.1 Uv-Vis Measurements

UV-Vis was carried out on the complete solar cells, in order to determine the absorbance of the complete ITO/cp-TiO_2/$CH_3NH_3PbI_3$/P3HT/Au, ITO/mp-TiO_2/$CH_3NH_3PbI_3$, ITO/cp-TiO_2/mp-TiO_2/$CH_3NH_3PbI_3$/P3HT/Au and ITO/PEDOT:PSS/$CH_3NH_3PbI_3$/PCBM/Au PSCs. This can give insights into a device's performance such as why one device architecture performs better than another. Measurements were carried out using a Cary 5G spectrophotometer. Uv-Vis measurements can also be used as an indication of the bandgap of a semiconductor based on the range of photons absorbed.

CHAPTER 4

RESULTS AND DISCUSSION

4.1 TiO_2 ETLs

$CH_3NH_3PbI_3$ PSCs which make use of either mp-TiO_2, cp-TiO_2, or a combination of the two have been widely explored in the literature related to PSCs [23,39,49,51,55,56]. However, the main focus of other researchers has been on improving the PCE of PSCs, with little focus on the phenomenon of hysteresis. It has been previously observed that ITO/cp-TiO_2/mp-TiO_2/$CH_3NH_3PbI_3$/P3HT/Au PSCs display reduced hysteresis as compared to ITO/cpTiO_2/$CH_3NH_3PbI_3$/P3HT/Au PSCs [21,23,49,57]. This indicates that mp-TiO_2 plays a significant role in the reduction of hysteresis. This work explored this point and found further evidence to support this claim.

Table 4.1. A comparison of the best performing ITO/cpTiO_2/$CH_3NH_3PbI_3$/P3HT/Au, ITO/cpTiO_2/mp-TiO_2/$CH_3NH_3PbI_3$/P3HT/Au, and ITO/cpTiO_2/mp-TiO_2/$CH_3NH_3PbI_3$/P3HT/Au PSCs.

	ITO/cp-TiO_2/ /$CH_3NH_3PbI_3$/P3HT/Au		**ITO/mpTiO_2/ /$CH_3NH_3PbI_3$/P3HT/Au**		**ITO/cp-TiO_2/mp-TiO_2/$CH_3NH_3PbI_3$/P3HT/Au**	
	Forward Voltage Scan	**Reverse Voltage Scan**	**Forward Voltage Scan**	**Reverse Voltage Scan**	**Forward Voltage Scan**	**Reverse Voltage Scan**
J_{SC}	1.08mA/cm^2	1.92mA/cm^2	2.19mA/cm^2	2.62mA/cm^2	7.17mA/cm^2	7.17mA/cm^2
V_{OC}	0.355V	0.558V	0.449V	0.425V	0.743V	0.823V
J_{MPP}	0.56mA/cm^2	1.78mA/cm^2	1.31mA/cm^2	1.73mA/cm^2	4.93mA/cm^2	6.20mA/cm^2
V_{MPP}	0.185V	0.265V	0.286V	0.282V	0.522V	0.666V
Hysteresis (ΔJ)	1.22mA/cm^2		0.42mA/cm^2		1.27mA/cm^2	
p	0.315		0.76		0.795	
Efficiency	0.104%	0.473%	0.373%	0.490%	2.57%	4.13%
Average efficiency	0.289%		0.432%		3.35%	

4.1.1 Hysteretic Behaviour and PCE of ITO/cp-TiO_2/$CH_3NH_3PbI_3$/P3HT/Au PSC

Table 5.1 outlines the measurements obtained during J-V testing of devices which made use of different TiO_2 ETLs. This information, in addition to giving a general overview of the performance of the PSCs fabricated, gives an overview of the hysteretic behaviour of the PSCs fabricated. The UV-Vis measurements taken provide information the variation of the PCEs. It should be noted that the absorbance measurements taken in this work are overestimated due to the beam width of the Cary 5G spectrophotometer being wider than the sample holder slit width. This meant that the beam made contact with a portion of the sample holder which is black. However, all measurements were equally overestimated and the trends are relevant.

The ITO/cp-TiO_2/$CH_3NH_3PbI_3$/P3HT/Au PSCs exhibited the lowest average PCE of 0.289 %. The $\dot{p}$ value for this PSC structure was determined to be 0.315. The J_{MPP} value for the reverse-scan curve was 1.78 mA/cm^2, while for the forward-scan curve it was 0.560 mA/cm^2. These values were both lower than the corresponding values for the other PSC structures studied. To gain insight into the lower PCE values, it is useful to examine the UV-Vis absorbance measured, since the amount of light absorbed by a solar cell will affect the efficiency as illustrated in Equation 2.21. The UV-Vis absorbance is displayed in Figure 4.4. It can be observed that the absorbance measured for this structure was consistently lower than that of the ITO/cp-TiO_2/mp-TiO_2/$CH_3NH_3PbI_3$/P3HT/Au PSCs in the wavelength region of 500-800 nm. However, although the absorbance was higher than that of the ITO/mp-TiO_2/$CH_3NH_3PbI_3$/P3HT/Au PSC from around 650-750 nm, the PCE was still lower. This can be attributed to pinholes in the $CH_3NH_3PbI_3$ film formed on top of the cp-TiO_2. It has proven difficult to deposit $CH_3NH_3PbI_3$ films on a layer of cp-TiO_2 without pinholes. This is made clear in the work carried out by other researchers [58–60]. It is therefore expected that due to the presence of pinholes that this PSC structure would have lower absorbance than the ITO/cp-TiO_2/mp-TiO_2/$CH_3NH_3PbI_3$/P3HT/Au PSC. This was also expected in the case of ITO/mp-TiO_2/$CH_3NH_3PbI_3$/P3HT/Au PSC, but did not hold true. Regardless, a lower PCE for the ITO/cp-TiO_2/$CH_3NH_3PbI_3$/P3HT/Au PSC was measured. Due to the presence of pinholes, the opportunity arose for the ITO to come into direct contact with the P3HT HTL. This caused a decrease in the shunt resistance, effectively lowering the MPP and resulting in a lower PCE. Table 5.1 also gives an overview of the hysteretic J-V behaviour displayed. As seen in Figure 4.3, it can be observed that J_{MPP} value for the reverse curve was 1.78 mA/cm^2, while the value for the forward curve was 0.56 mA/cm^2 which gave rise to ΔJ = 1.22 mA/cm^2 and $\dot{p}$ = 0.315, which means that ITO/cp-

$TiO_2/CH_3NH_3PbI_3$/P3HT/Au PSCs exhibited the largest variation between its forward and reverse curves.

Jiang *et al.* [37] found that the depletion region due to the p-n junction formed as a result of the TiO_2 and $CH_3NH_3PbI_3$ interface was ≈300 nm. This means that if the $CH_3NH_3PbI_3$ layer of a PSC is within 300 nm of the $CH_3NH_3PbI_3$/cp-TiO_2 (ITO) interface, then a significant amount of I^- ions can be drifted to this location, subsequently reducing the V_{OC}, J_{SC}, and therefore the PCE of the PSC when the light up J-V curve is measured, as outlined in Chapter 3. Figure 4.2 a) gives an estimate of the location and width of the depletion zone of the ITO/cp-$TiO_2/CH_3NH_3PbI_3$/P3HT/Au PSC based on the report by Jiang et al. [37]. SEM images allow for the estimation of the thicknesses of the various layers of a PSC. In this work, this means that based on the thicknesses derived from the SEM images, it can be determined how likely it is for I^- ion accumulation at the $CH_3NH_3PbI_3$/cp-TiO_2 (ITO) interface, considering a depletion width of around 300 nm. Figure 4.2 a) shows that for a cp-$TiO_2/CH_3NH_3PbI_3$ film on an Ossila® ITO substrate, there is a cp-TiO_2 layer which is about 13 nm in thickness, while the $CH_3NH_3PbI_3$ is around 360 nm thick. The built-in field E_0 encompasses the majority of the cp-TiO_2 and $CH_3NH_3PbI_3$ layers. Based on the direction of the field, I^- ions can be drifted to the cp-$TiO_2/CH_3NH_3PbI_3$ interface. This results in a modulation of the built-in field (E_0) at the p-n junction as described in Section 3.4. Due to the electric field, E_A, which develops in opposition of the field due to the p-n junction, the number of electrons which can be extracted to an external circuit are reduced. This leads to reduced photovoltaic performance of the forward-scan J-V curve in comparison to the reverse-scan J-V curve as pictured in Figure 4.2 b).

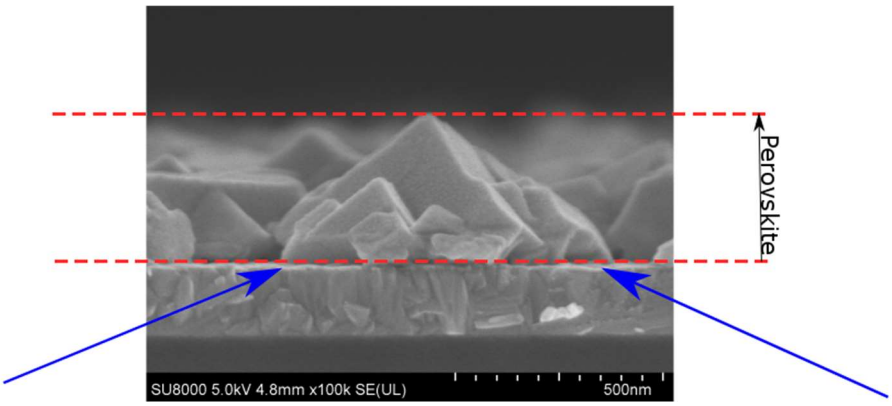

Figure 4.1. SEM micrograph of an ITO/ cp-$TiO_2/CH_3NH_3PbI_3$ film. The blue arrows indicate the thin cp-TiO_2 layer.

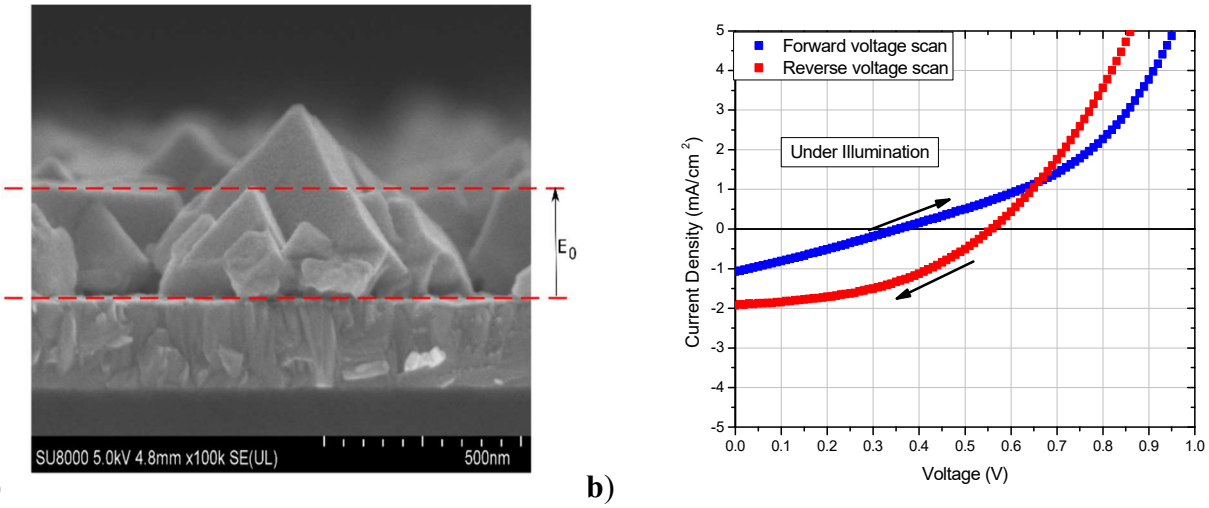

Figure 4.2. a) A spatial representation of the electric field which arises as a result of the p-n junction formed at the cp-TiO_2/$CH_3NH_3PbI_3$ interface of an ITO/cp-TiO_2/$CH_3NH_3PbI_3$/P3HT/Au PSC. b) J-V curves of an ITO/cp-TiO_2/$CH_3NH_3PbI_3$/P3HT/Au PSC.

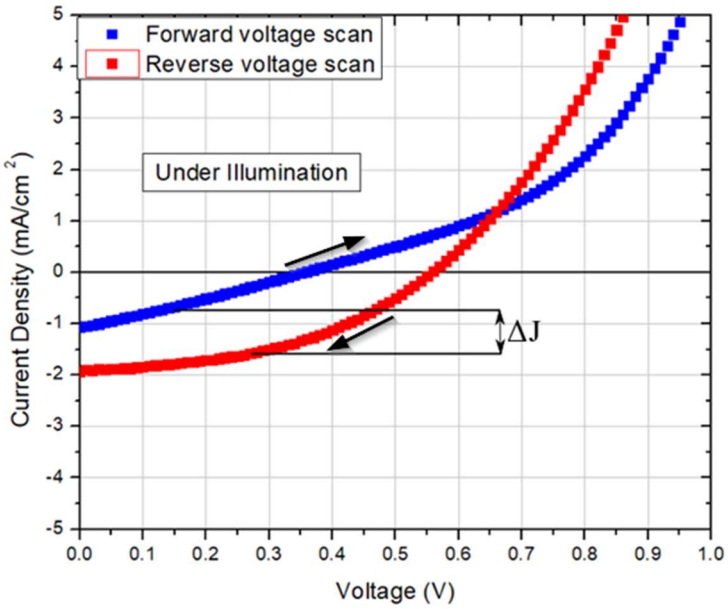

Figure 4.3. The difference between the maximum power points of the light up and light down curves of the ITO/cp-TiO_2/$CH_3NH_3PbI_3$/P3HT/Au PSC.

4.1.2 Hysteretic Behaviour and PCE of ITO/mp-TiO_2/$CH_3NH_3PbI_3$/P3HT/Au PSC

The average PCE of the ITO/mp-TiO_2/$CH_3NH_3PbI_3$/P3HT/Au PSC was 0.473%. This is larger than that of the ITO/cp-TiO_2/$CH_3NH_3PbI_3$/P3HT/Au PSC but not by a significant margin. The ITO/mp-TiO_2/$CH_3NH_3PbI_3$/P3HT/Au PSC, also exhibited reduced absorbance as compared to the ITO/cp-TiO_2/$CH_3NH_3PbI_3$/P3HT/Au PSC in the 650-750 nm region. This is unexpected since the mp-TiO_2 scaffold is expected to support the growth of uniform $CH_3NH_3PbI_3$ films in devices which have this layer, resulting in increased values of absorbance and aiding in the photovoltaic performance [30, 68, 69]. However, this is not reflected in the measured absorbance. The reduced PCE as compared to the ITO/cp-TiO_2/mp-TiO_2/$CH_3NH_3PbI_3$/P3HT/Au PSC is to be expected however, since pathways where the mp-TiO_2 layer simply connects the ITO and the P3HT are likely due to its porosity [43, 70]. Such pathways decrease the shunt resistance in PSCs and result in lower PCE values. The reduced absorbance could be attributed to a fault in the deposition of the $CH_3NH_3PbI_3$ layer of the ITO/mp-TiO_2/$CH_3NH_3PbI_3$/P3HT/Au PSCs during spin-coating.

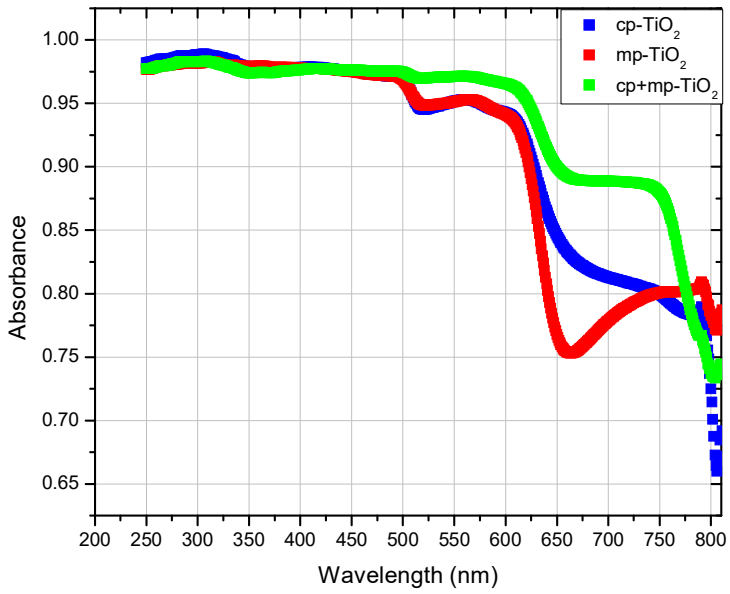

Figure 4.4. UV-Vis spectra for ITO/cp-TiO_2/$CH_3NH_3PbI_3$/P3HT/Au, ITO/mp-TiO_2/$CH_3NH_3PbI_3$/P3HT/Au, and ITO/cp-TiO_2/mp-TiO_2/$CH_3NH_3PbI_3$/P3HT/Au PSCs.

It can be seen in Figure 4.3 that the J_{MPP} for the reverse voltage scan curve was 1.73 mA/cm^2, while for the forward voltage scan curve it was 1.31 mA/cm^2. This gave rise to a p value of 0.76.

Although a mp-TiO_2/$CH_3NH_3PbI_3$ film was not made to be analyzed via an SEM image, the cp-TiO_2/mp-TiO_2/$CH_3NH_3PbI_3$ pictured in Figure 4.6 and Figure 5.7 can be used to gain an idea of what should have occurred. The mp-TiO_2 layer of the cp-TiO_2/mp-TiO_2/$CH_3NH_3PbI_3$ film was approximately 315 nm thick, while the $CH_3NH_3PbI_3$ capping layer was approximately 133 nm thick. The ITO/mp-TiO_2/$CH_3NH_3PbI_3$/P3HT/Au PSC was fabricated in the same way as ITO/cp-TiO_2/mp-TiO_2/$CH_3NH_3PbI_3$/P3HT/Au PSC, so these values will be assumed to hold true for the PSC without the cp-TiO_2 layer. Jiang *et al.*observed that there are 2 built-in fields in an ITO/cp-TiO_2/mp-TiO_2/$CH_3NH_3PbI_3$/2,20,7,70-tetrakis(N,N-dip-methoxyphenylamine)-9,90-spiro-bifluorene (spiro-MeOTAD)/Ag PSC. The energy level diagram in Figure 4.5 shows that this PSC functions similarly to those fabricated in this work.

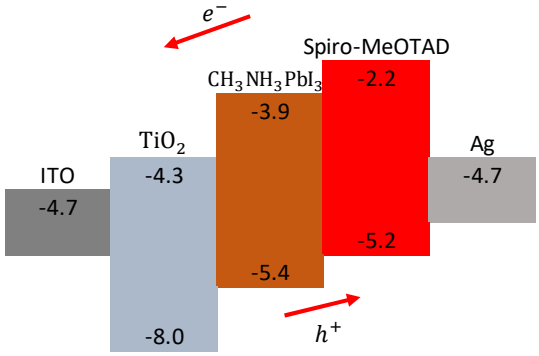

Figure 4.5. Energy Level Diagram of the ITO/cp-TiO_2/mp-TiO_2/$CH_3NH_3PbI_3$/spiro-MeOTAD/Ag PSC fabricated by Jiang *et al.* [37].

It is therefore expected that the proposed electric fields were also present in the ITO/mp-TiO_2/$CH_3NH_3PbI_3$/P3HT/Au PSCs fabricated in this work. Figure 5.7 displays a representation of the electric fields which were expected to be present in the ITO/mp-TiO_2/$CH_3NH_3PbI_3$/P3HT/Au PSC, as well as the corresponding J-V curves. The electric fields are a result of the $CH_3NH_3PbI_3$ layer forming a p-n junction with the mp-TiO_2 layer, as well as due to a p-n junction with the ITO and the $CH_3NH_3PbI_3$ which infiltrated the porous TiO_2 network in ITO/cp-TiO_2/mp-TiO_2/$CH_3NH_3PbI_3$/P3HT/Au PSCs. This is possible since ITO is an n-type semiconductor [29]. It is likely that there was more $CH_3NH_3PbI_3$ in the capping layer than within the porous TiO_2 network since the PbI_2 and CH_3NH_3I solutions were not allowed to settle on the mp-TiO_2 layer since they were dynamically spin-coated. On hitting the mp-TiO_2, the majority of these solutions would have

been flung off with most of the remainder forming the capping layer and a minimal amount infiltrating the mp-TiO_2 layer. This resulted in the $CH_3NH_3PbI_3$ within the mp-TiO_2 essentially forming a lightly doped p-type (p^-) layer [37]. This means that there was an electric field formed at the ITO/mp-TiO_2 interface due to a p^--n junction, and a field at the interface of the mp-TiO_2 and $CH_3NH_3PbI_3$ capping layer due to the p-n junction formed there. There was reduced ion accumulation due to what is effectively a p^- layer within the mp-TiO_2 at the ITO/mp-TiO_2 + $CH_3NH_3PbI_3$ interface, since there was a reduced amount of $CH_3NH_3PbI_3$, and therefore less I^- ions. The field due to the p-n junction with the mp-TiO_2 + $CH_3NH_3PbI_3$/$CH_3NH_3PbI_3$ capping layer interface was unable to drift I^- ions near the cp-TiO_2/mp-TiO_2 + $CH_3NH_3PbI_3$ interface since the electric field does not cover a wide enough thickness of the PSC to do so since the combined thickness of the $CH_3NH_3PbI_3$ capping layer and the mp-TiO_2 + $CH_3NH_3PbI_3$ layer was around 450 nm thick. This results in the reduced hysteresis observed in ITO/mp-TiO_2/$CH_3NH_3PbI_3$/P3HT/Au PSCs.

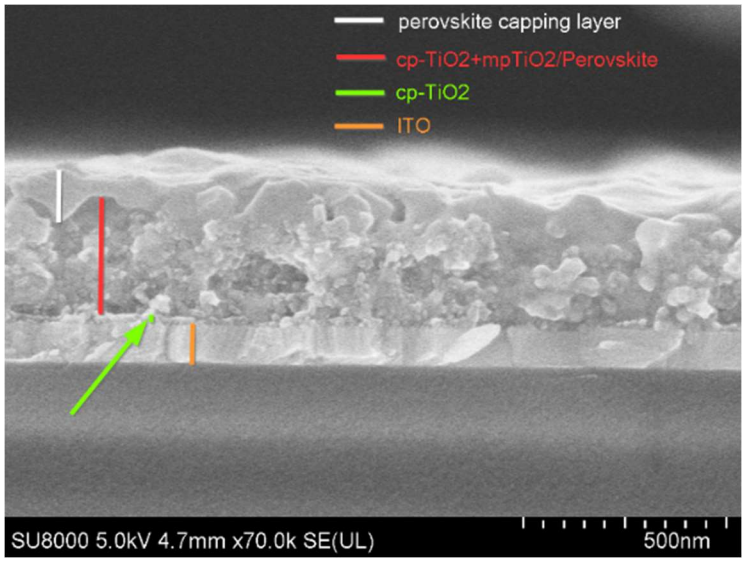

Figure 4.6. SEM micrograph of an ITO/cp-TiO_2/mp-TiO_2/$CH_3NH_3PbI_3$ film

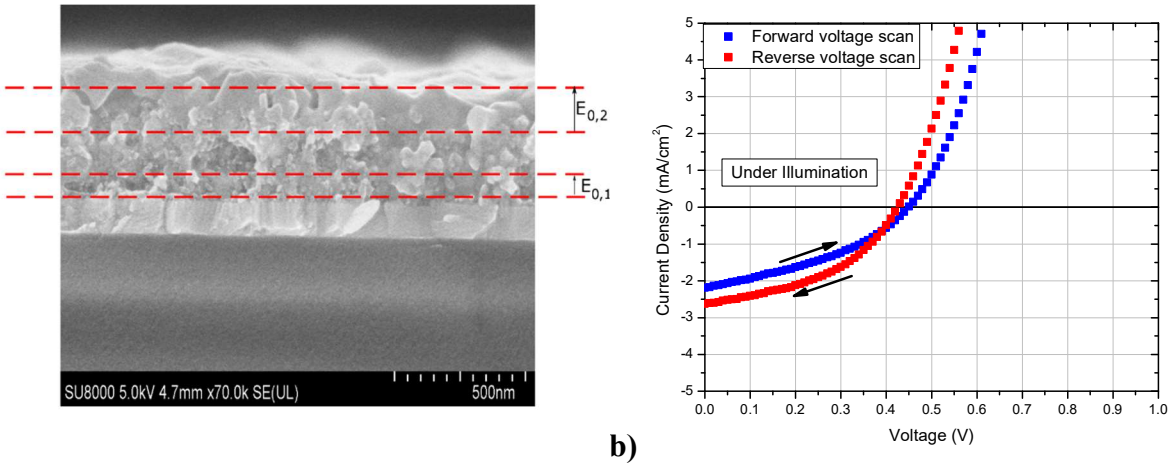

a) b)

Figure 4.7. a) A spatial representation of the electric fields which arise as a result of the p-n junctions formed in devices with a mp-TiO_2 layer. b) J-V curves of an ITO/mp-TiO_2/$CH_3NH_3PbI_3$/P3HT/Au PSC.

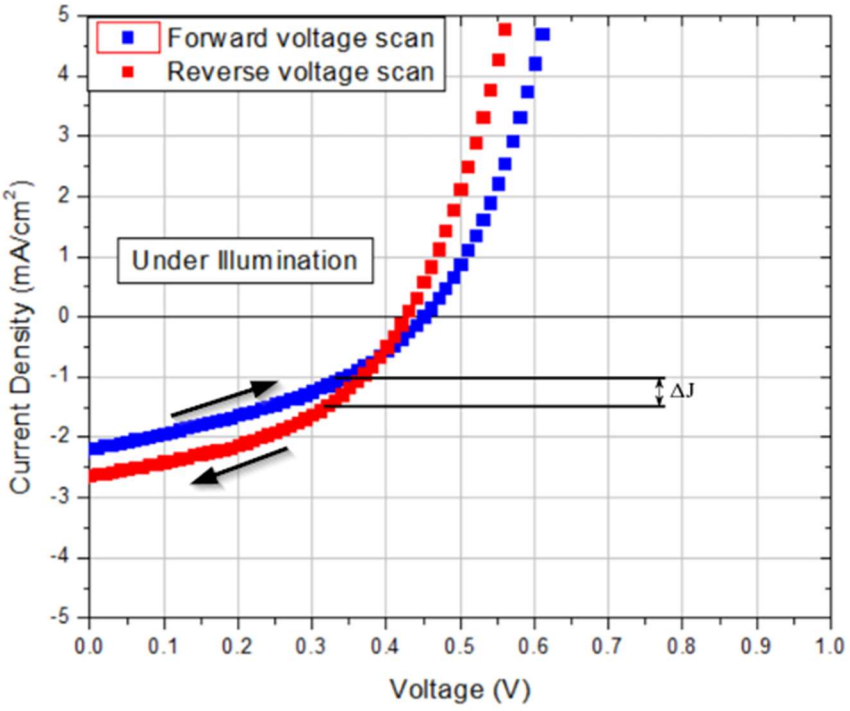

Figure 4.8. The difference between the maximum power points of the light up and light down curves of the ITO/mp-TiO_2/$CH_3NH_3PbI_3$/P3HT/Au PSC.

4.1.3 Hysteretic Behaviour and PCE of ITO/cp-TIO$_2$/mp-TiO$_2$/CH$_3$NH$_3$PbI$_3$/P3HT/Au PSC

The hysteretic behaviour of the ITO/cp-TiO$_2$/mp-TiO$_2$/CH$_3$NH$_3$PbI$_3$/P3HT/Au PSC was quite similar to that of the ITO/mp-TiO$_2$/CH$_3$NH$_3$PbI$_3$/P3HT/Au PSC. This is shown in the similar p value of 0.795. However in such a PSC, the cp-TiO$_2$ layer prevents short-circuits between the P3HT HTL and the ITO [36,48]. This results in an increased shunt resistance. It does not appear that any spin-coating errors were made either, and the ITO/cp-TiO$_2$/mp-TiO$_2$/CH$_3$NH$_3$PbI$_3$/P3HT/Au PSCs exhibited higher absorbance values in the 500-800 nm wavelength region. These factors result in the ITO/cp-TiO$_2$/mp-TiO$_2$/CH$_3$NH$_3$PbI$_3$/P3HT/Au PSC having higher values of p and PCE. The average PCE value is listed in Table 1 and on examining Figure 4.9, it can be seen that the J_{MPP} value for the reverse voltage scan curve was 6.20 mA/cm^2, while the J_{MPP} value for the forward voltage scan curve was 4.93 mA/cm^2 which gave rise to ΔJ = 1.27 mA/cm^2, and p = 0.795, which means that ITO/cp-TiO$_2$/CH$_3$NH$_3$PbI$_3$/P3HT/Au PSCs exhibited the smallest variation between its forward and reverse voltage curves among the PSCs fabricated with TiO$_2$ ETLs.

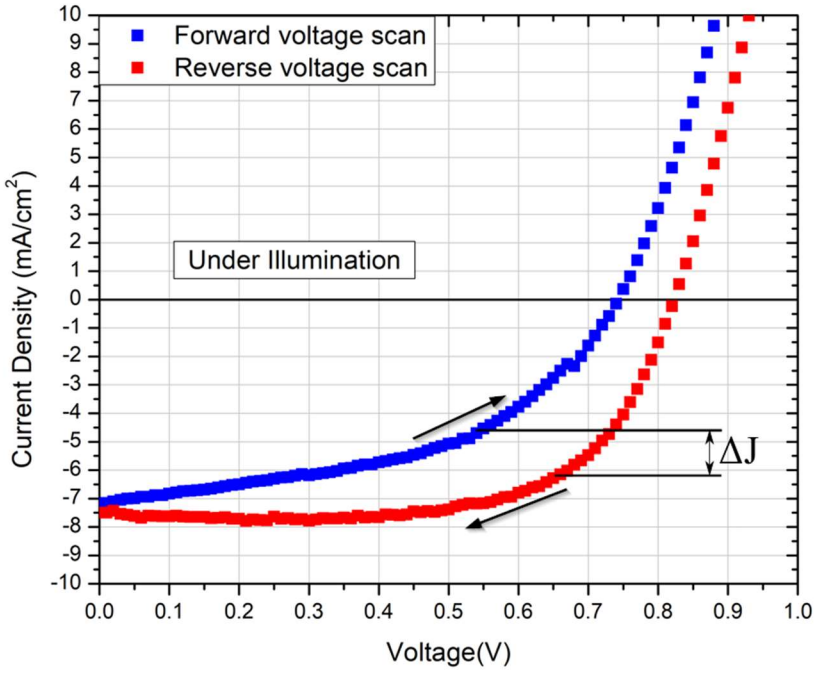

Figure 4.9. The difference between the maximum power points of the light up and light down curves of the ITO/cp-TiO$_2$/mp-TiO$_2$/CH$_3$NH$_3$PbI$_3$/P3HT/Au PSC.

4.1.4 Overview of TiO_2 based PSCs

The mp-TiO_2 layer provided structural support for the formation of a more uniform $CH_3NH_3PbI_3$ layer as compared to the PSC which make use of only cp-TiO_2. This allowed for increased absorbance in the ITO/cp-TiO_2/mp-TiO_2/$CH_3NH_3PbI_3$/P3HT/Au PSC. Unfortunately, this increased absorbance was not realized in the ITO/mp-TiO_2/$CH_3NH_3PbI_3$/P3HT/Au PSC counterparts. The thickness of the mp-TiO_2 layer, in addition to that of the $CH_3NH_3PbI_3$ capping layer, which was around 450 nm, meant that a significant amount of I^- ions could not be drifted by the electric fields present in the PSCs fabricated in this work which contained mp-TiO_2. However, in the case of the ITO/cp-TiO_2/$CH_3NH_3PbI_3$/P3HT/Au PSC, the $CH_3NH_3PbI_3$ layer is around 360 nm thick, which meant that the electric field formed encompassed most of this layer and was able to drift a much larger amount of I^- ions to the cp-TiO_2/$CH_3NH_3PbI_3$ interface. For this reason the ITO/cp-TiO_2/$CH_3NH_3PbI_3$/P3HT/Au PSC displayed the lowest *ƥ* value. The PCE was also lower than the PSCs containing mp-TiO_2. While based on the argument presented it is expected that a thicker mp-TiO_2 layer should further decrease the level of observed hysteresis, it should be noted that it has been observed that on continually increasing the mp-TiO_2 layer thickness, the PCE of the PSC in question begins to drop off. This is due to the high resistance of TiO_2 [55,64,65]. Therefore, the thickness of the mp-TiO_2 layer should be optimized in order to maximize PCEs while decreasing hysteresis in $CH_3NH_3PbI_3$-based PSCs with TiO_2 ETLs. It should be noted that by isolating mp-TiO_2 in a device on its own, this work highlighted that mp-TiO_2 plays a significant role in the reduction of hysteresis since similar values of *ƥ* were obtained, even in the mp-TiO_2 PSC fabricated without a cp-TiO_2 layer present.

Note that Jiang *et al.* found that the HTL had a trivial effect on the electric fields due to p-n junctions in their TiO_2 based PSCs. They demonstrated this by fabricating PSCs without HTLs, which when tested, were shown to have electric fields of similar strength to devices fabricated with HTLs [37]. For this reason, SEM images were taken of the relevant device structures without the HTLs and Au electrodes, since this was unnecessary for the purpose of the measurement taken and would have also been time consuming. This also further strengthens the argument that mp-TiO_2 is responsible for the reduced hysteresis observed in PSCs making use of mp-TiO_2 ETLs as compared to those making use of cp-TiO_2 ETLs.

4.2 PCBM ETL

The observed hysteresis in $CH_3NH_3PbI_3$ PSCs can be explained by mobile I^- ions which drift to the cp-TiO_2/$CH_3NH_3PbI_3$ interface in the case of ITO/cp-TiO_2/mp-TiO_2/$CH_3NH_3PbI_3$/P3HT/Au PSCs and the ITO/mp-TiO_2 interface in the case of ITO/mp-TiO_2/$CH_3NH_3PbI_3$/P3HT/Au PSCs. These ions are drifted by an electric field which acts in opposition to the motion of photoexcited charge carriers, reducing the PCE in the forward J-V scan direction. The electric field occurs due to the formation of a p-n junction at the cp-TiO_2/$CH_3NH_3PbI_3$ (ITO/mp-TiO_2) interface. Without this electric field, there should be no hysteresis. In order to investigate this further, it is useful to examine the case of a PSC structure where no p-n junction is formed.

In order to gain further insight into how a $CH_3NH_3PbI_3$ PSC is expected to function, it is useful to briefly examine the function of an organic solar cell. Although the same general mechanism of charge transport applies to $CH_3NH_3PbI_3$ PSCs, it should be noted that EHPs are generated directly in PSCs [34,66]. In organic solar cells, EHPs are not generated. Instead, tightly bound excitons are generated [67,68]. One approach to fabricating organic solar cells is sandwiching an organic material between a cathode and an anode. This produces inefficient solar cells however, since excitons can only be dissociated into an EHP by the electric field which occurs due to the difference in work function of the electrodes [67]. This electric field is too weak to successfully dissociate a significant number of excitons into EHPs. However, this is necessary for electrons to be extracted to an external circuit to do useful work.

A more successful approach to making an organic solar cell is to form a heterojunction between a hole transporting organic donor and an electron transporting organic acceptor material. A strong electric field is formed at this junction, which facilitates more effective exciton dissociation. This electric field is highly localized and only spans a region which does not extend far outside a few nm of the heterojunction interface [68]. Although this increases the number of charge carriers which can contribute to the photocurrent, the PCE of this type of solar cell is still relatively low. Organic solar cells are hampered by short diffusion lengths of only around 10 nm [67,68], limiting the range of photons that can be absorbed and ultimately their PCEs, since these devices must be quite thin, in order to avoid significant recombination which will begin to occur in devices much thicker than 10 nm.

In this work, it was assumed that the highly localized electric field formed at a junction with an organic semiconducting material would not pose a large challenge in terms of reducing the PCE of a $CH_3NH_3PbI_3$ PSC. Therefore, an organic ETL in the form of PCBM and an organic HTL in the form of PEDOT:PSS were employed. This type of PSC has a diffusion length, on the order of 1000 nm [15], and an absorption coefficient on the order of 1.5×10^4 photons/cm at 500 nm and 0.5×10^4 photons/cm at 700 nm [69]. This means that these PSCs can be made thick enough to absorb as much light as possible, while still operating without crippling recombination due to a device whose thickness far outstrips the limitations imposed by the diffusion lengths of its charge carriers. In PSC structures such as those which make use of TiO_2, or inorganic silicon solar cells, carriers generated within the region which consists of the depletion region, in addition to the diffusion lengths of the charge carriers can be extracted to an external circuit to do useful work. Essentially, this means that only charge carriers generated within the distance $L_h + W + L_e$, where L_h, W and L_e are the hole diffusion length, depletion region width, and electron diffusion length respectively, contribute to the photocurrent [16]. However, the absence of W as a result of the formation of a p-n junction does not mean that the performance of a $CH_3NH_3PbI_3$ PSC making use of organic transport layers will be hampered. Relatively efficient transport of carriers to the electrodes via the ETLs and HTLs is still expected to occur with minimal hysteresis, in a $CH_3NH_3PbI_3$ PSC, making use of organic ETLs and HTLs. Even though there is no W contribution, the diffusion length of a $CH_3NH_3PbI_3$ PSC making use of organic HTLs and/or ETLs is still over 1 μm and the performance should not be hampered. The thickness of such a PSC is expected to be similar to that of the ITO/cp-TiO_2/$CH_3NH_3PbI_3$/P3HT/PCBM/Au PSC due to the use of the same fabrication method. This gives an estimated thickness of around 360 nm. This means that a large amount of generated carriers can still be collected. Organic transport layers will result in localized electric fields centred around the interface of the $CH_3NH_3PbI_3$ which means that a significant amount of mobile I^- ions cannot be drifted.

Table 4.2. Performance of ITO/PEDOT:PSS/$CH_3NH_3PbI_3$/PCBM/Au PSC fabricated in this work.

	Up	Down
J_{SC}	7.49 mA/cm^2	7.55 mA/cm^2
V_{OC}	0.872	0.953
J_{MPP}	5.29 mA/cm^2	5.35 mA/cm^2
V_{MPP}	0.429	0.453
Hysteresis (ΔJ)	0.06 mA/cm^2	
þ	0.989	
Efficiency	2.27 %	2.42 %
Average efficiency	2.35 %	

The results obtained after carrying out J-V measurements on the ITO/PEDOT:PSS/$CH_3NH_3PbI_3$/Au PSCs fabricated in this work, corroborate this. The devices displayed an average PCE of 2.35 % with a *þ* value of 0.989. This meant that the ITO/PEDOT:PSS/$CH_3NH_3PbI_3$/Au PSC exhibited the most stable power output when compared to all other PSC structures fabricated. Figure 4.10 demonstrates the close proximity of the forward voltage scan and reverse voltage scan J-V curves.

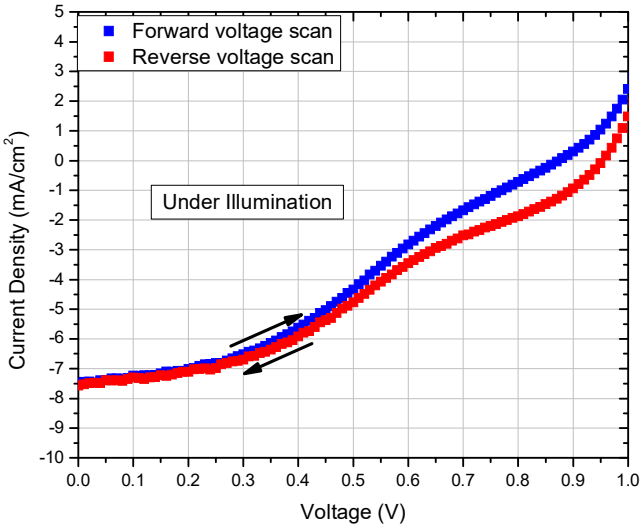

Figure 4.10. J-V Characteristics of ITO/PEDOT:PSS/$CH_3NH_3PbI_3$/PCBM/AU PSC

From observing Figure 4.11, it should also be noted that while the absorbance of the ITO/PEDOT:PSS/$CH_3NH_3PbI_3$/PCBM/Au PSC was higher than the ITO/cp-TiO_2/mp-TiO_2/$CH_3NH_3PbI_3$/P3HT/Au PSC in the 600-800 nm wavelength region, it was lower in the higher energy 500-650 nm region. This could possibly also have contributed to the lower PCE observed.

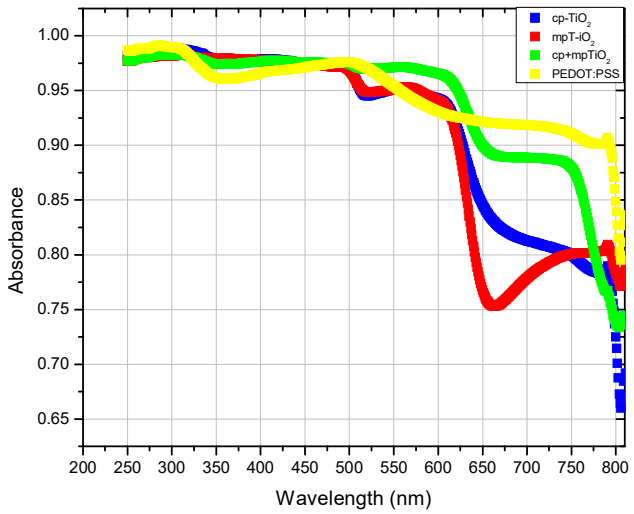

Figure 4.11. UV-Vis Absorbance Characteristics of ITO/PEDOT:PSS/$CH_3NH_3PbI_3$/Au PSC

4.3 Conclusions

The UV-Vis measurements show a sharp increase in absorbance around 806 nm which agrees with the bandgap of around 1.54 eV reported in the literature for $CH_3NH_3PbI_3$ PSCs [23,63,70–74]. It is important to take such a measurement for a $CH_3NH_3PbI_3$ PSC since they can degrade quite quickly [75–77] unless measures such as encapsulation and storage in a N_2 environment are taken. When these devices start to degrade, PbI_2 is reformed and would expected to make a larger contribution to the UV-Vis spectra. This would essentially mean that a narrower spectrum would be expected since PbI_2 has a larger bandgap and thus only absorbs a smaller, higher energy portion of visible photons [77]. This was not the case in this work and the spectra were as expected. These were indeed $CH_3NH_3PbI_3$ PSCs which underwent little to no degradation after fabrication. This was confirmed by the UV-Vis measurements which were taken 1 week after J-V testing after being stored in a N_2 glovebox.

While the use of mp-TiO_2 as an ETL/scaffold in $CH_3NH_3PbI_3$ PSCs reduces hysteresis, a layer of cp-TiO_2 in addition to the mp-TiO_2 is required to reap the benefits of both decreased hysteresis and increased PCE as compared to PSCs using solely a layer of cp-TiO_2 as an ETL. The mp-TiO_2 helps to mitigate the effects of the electric field which results due to a p-n junction formed at the cp-TiO_2 (or ITO)/$CH_3NH_3PbI_3$ interface. By reducing the effect of this electric field, the drift of I^- ions to the interface is reduced. On the other hand in the ITO/PEDOT:PSS/$CH_3NH_3PbI_3$/PCBM/Au PSC, any electric fields at the PEDOT:PSS or the PCBM interface with the $CH_3NH_3PbI_3$ will be highly localized and unable to drift a significant amount of I^- ions. This is reflected in the experimentally determined þ value of 0.989 for the ITO/PEDOT:PSS/$CH_3NH_3PbI_3$/PCBM/Au PSC. It should be noted however, that if pinholes are present in an organic transport layer which contacts the ITO layer, this could mean that the portion of exposed ITO will form a p-n junction the $CH_3NH_3PbI_3$ layer. This would result in undesirable hysteretic J-V behaviour. However, with this in mind, organic ETLs are prime candidates for reducing hysteresis in $CH_3NH_3PbI_3$ PSCs since their use strongly appears to improve the stability of the power output of $CH_3NH_3PbI_3$ PSCs.

CHAPTER 5

SUMMARY AND FUTURE WORK

5.1 Summary

Given the objectives set out, the following should be noted:

- J-V hysteresis in PSCs which make use of TiO_2 as an ETL occurs due to an electric field because of a p-n junction at the $TiO_2/CH_3NH_3PbI_3$ interface. This electric field drifts I^- ions to the $TiO_2/CH_3NH_3PbI_3$ interface and reduces the amount of electrons that can be extracted to an external circuit to do useful work.
- Using an organic material as an ETL should result in negligible hysteresis since no p-n junction can be formed at the ETL/$CH_3NH_3PbI_3$ interface in such a device. In order to test that this is indeed true, an ITO/PEDOT:PSS/$CH_3NH_3PbI_3$/PCBM/Au PSC was fabricated and its J-V hysteretic behaviour observed. This PSC structure as fabricated in this work displayed negligible J-V hysteresis. A lower average efficiency than the ITO/cp-TiO_2/mp-TiO_2/$CH_3NH_3PbI_3$/P3HT/Au PSC was observed but Heo et. al. [53] reported an efficiency of 18.1% which suggests that higher efficiencies can be gained given more sterile fabrication conditions than were possible in this work.

The origin of hysteresis in $CH_3NH_3PbI_3$-based PCSs with compact and/or mesoporous TiO_2 ETLs has been investigated. Solar cells with the structure ITO/cp-TiO_2/$CH_3NH_3PbI_3$/P3HT/Au, ITO/mp-TiO_2/$CH_3NH_3PbI_3$/P3HT/Au, ITO/cp-TiO_2/mp-TiO_2/$CH_3NH_3PbI_3$/P3HT/Au, and ITO/ PEDOT:PSS/$CH_3NH_3PbI_3$/PCBM/Au were fabricated using a combination of deposition methods: spin coating for deposition of the ETLs, the $CH_3NH_3PbI_3$ active layer and the HTLs, and thermal evaporation for the Au electrodes. The PSCs were encapsulated after the electrode deposition in order to prevent the ingress of air and moisture which could damage $CH_3NH_3PbI_3$ films quickly, drastically reducing their performance. The connection legs were attached after encapsulation which allowed for J-V testing to be carried out more easily.

The *J-V* measurements were taken in order to determine the PCEs of the solar cells investigated. The ITO/cp-TiO_2/mp-TiO_2/$CH_3NH_3PbI_3$/P3HT/Au structure displayed the highest average PCE of 3.35%. The ITO/cp-TiO_2/$CH_3NH_3PbI_3$/P3HT/Au had an average PCE of 0.432%, while the ITO/cp-TiO_2/CH3NH3PbI3/P3HT/Au structure had an average PCE of 0.289%. The mp-TiO_2

scaffold facilitated higher quality $CH_3NH_3PbI_3$ film formation, which allowed for increased light absorption as compared to the structure using just cp-TiO_2. This explains why the ITO/cp-TiO_2/mp-TiO_2/$CH_3NH_3PbI_3$/P3HT/Au PSCs had the greatest PCE. However, the ITO/mp-TiO_2/$CH_3NH_3PbI_3$/P3HT/Au structure did not show a significantly improved PCE as compared to the ITO/cp-TiO_2/$CH_3NH_3PbI_3$/P3HT/Au. The absorbance measurements of the ITO/mp-TiO_2/$CH_3NH_3PbI_3$/P3HT/Au also do not show increased absorbance compared to the ITO/cp-TiO_2/$CH_3NH_3PbI_3$/P3HT/Au structure. The lower than expected absorbance can be attributed to a possible error in the $CH_3NH_3PbI_3$ spin-coating and formation procedure. In addition due to the lack of a cp-TiO_2 layer and due to the porous nature of the mp-TiO_2, it is possible in some areas that the HTL was directly connected to the ITO of the Ossila® substrate. This would have resulted in a short-circuit in some areas of the PSC in question and reduced the PSC performance.

SEM images of the TiO_2 structures investigated allowed for the investigation of the location of drifting I^- ions based. These images showed that it is possible for an electric field to drift ions to the cp-TiO_2/ $CH_3NH_3PbI_3$ interface in ITO/cp-TiO_2/$CH_3NH_3PbI_3$/P3HT/Au PSCs based on the width of the depletion region proposed by Jiang *et al.* [37]. In ITO/mp-TiO_2/$CH_3NH_3PbI_3$/ P3HT/Au and ITO/cp-TiO_2/mp-TiO_2/$CH_3NH_3PbI_3$/P3HT/Au PSCs, it is proposed that there are two electric fields set up. The electric field at the cp-TiO_2 (or ITO)/ $CH_3NH_3PbI_3$ interface should only cause the drift and accumulation of a limited number of halide ions. The electric field at the mp-TiO_2/ $CH_3NH_3PbI_3$ interface does not reach far enough into the device to drift ions to the interface of the $CH_3NH_3PbI_3$ interface with the cp-TiO_2 (or ITO). This ultimately results in the reduced hysteresis displayed by the PSC structures which made use of mp-TiO_2. The ITO/mp-TiO_2/$CH_3NH_3PbI_3$/P3HT/Au displayed a β value of 0.76, while the ITO/cp-TiO_2/mp-TiO_2/$CH_3NH_3PbI_3$/P3HT/Au PSC displayed a β value of 0.795. Based on evidence by Jiang *et al.* who carried out extensive profiling of the electric fields present in the PSC structures investigated in this work, the HTLs have little effect on the electric field profiles of these PSCs [37]. Since this research isolated mp-TiO_2 in a separate PSC without cp-TiO_2, it can be deduced that mp-TiO_2 plays a significant role in the reduced hysteresis observed in devices which make use of this material.

The electric field formed due to the p-n junction at the TiO_2 interface(s) of the PSCs making use of TiO_2 as an ETL in this work caused the observed hysteresis. ITO/PEDOT:PSS/ $CH_3NH_3PbI_3$/PCBM/Au PSCs will only have highly localized electric fields. This means that this

PSC structure will be unable to drift an amount of I^- ions significant enough to cause J-V hysteresis. This PSC structure had a *p* value of 0.989 which meant that it displayed the most stable power output.

5.2 Future Work

While mp-TiO_2 is shown to reduce J-V hysteresis in $CH_3NH_3PbI_3$ PSCs in this work, the migration of I^- ions has not been directly measured in an *in operando* PSC. This type of measurement is possible with the high intensity radiation available at a synchrotron facility via grazing incidence X-ray diffraction (GIXRD). It has previously been used at the Australian Synchrotron in Victoria, Australia to study the movement of lithium and sodium ions in lithium ion batteries by Pramudita *et al.* [78]. Such an experiment would help to clarify one of the more unclear aspects of $CH_3NH_3PbI_3$ PSCs and help to improve the fundamental understanding of this fledgling solar cell technology, ultimately allowing for a deeper insight into how to improve these devices and bring the technology closer to commercialization.

REFERENCES

[1] NASA's Jet Propulsion Laboratory, Global climate change vital signs of the planet: effects. https://climate.nasa.gov/effects/ (accessed July 14, 2017).

[2] P.U. Clark, A.C. Mix, Ice sheets and sea level of the Last Glacial Maximum, Quat. Sci. Rev. 21 (2002) 1–7. doi:10.1016/S0277-3791(01)00118-4.

[3] J. Cook, N. Oreskes, P.T. Doran, W.R.L. Anderegg, B. Verheggen, E.W. Maibach, J.S. Carlton, S. Lewandowsky, A.G. Skuce, A. Sarah, Consensus on consensus : a synthesis of consensus estimates on human - caused global warming, Environ. Res. Lett. 11 (2016) 1–24. doi:10.1088/1748-9326/11/4/048002.

[4] M. Cai, Y. Wu, H. Chen, X. Yang, Y. Qiang, L. Han, Cost-performance analysis of Perovskite solar modules, Adv. Sci. 4 (2017). doi:10.1002/advs.201600269.

[5] C. Smith, A.R. Barron, Synthesis and purification of bulk semiconductors. http://cnx.org/contents/Q8JC6j42@7/Synthesis-and-Purification-of- (accessed August 6, 2017).

[6] W. Huang, J.S. Manser, P. V. Kamat, S. Ptasinska, Evolution of chemical composition, morphology, and photovoltaic efficiency of CH3NH3PbI3 Perovskite under Ambient Conditions, Chem. Mater. 28 (2016) 303–311. doi:10.1021/acs.chemmater.5b04122.

[7] J. Seo, J.H. Noh, S. Il Seok, Rational strategies for efficient Perovskite solar cells, Acc. Chem. Res. 49 (2016) 562–572. doi:10.1021/acs.accounts.5b00444.

[8] X. Li, D. Bi, C. Yi, J.-D. Decoppet, J. Luo, S.M. Zakeeruddin, A. Hagfeldt, M. Gratzel, A vacuum flash-assisted solution process for high-efficiency large-area Perovskite solar cells, Science 8060 (2016) 1–10. doi:10.1126/science.aaf8060.

[9] M. Saliba, T. Matsui, J.-Y. Seo, K. Domanski, J.-P. Correa-Baena, N. Mohammad K., S.M. Zakeeruddin, W. Tress, A. Abate, A. Hagfeldt, M. Gratzel, Cesium-containing triple cation

Perovskite solar cells: improved stability, reproducibility and high efficiency, Energy Environ. Sci. 9 (2016) 1853-2160. doi:10.1039/C5EE03874J.

[10] A. Kojima, K. Teshima, Y. Shirai, T. Miyasaka, Organometal halide Perovskites as visible-light sensitizers for photovoltaic cells, J. Am. Chem. Soc. 131 (2009) 6050–6051. doi:10.1021/ja809598r.

[11] W. Tress, N. Marinova, T. Moehl, S.M. Zakeeruddin, N. Mohammad K., M. Grätzel, M.K. Nazeeruddin, M. Grätzel, Understanding the rate-dependent J–V hysteresis, slow time component, and aging in CH3NH3PbI3 Perovskite solar cells: the role of a compensated electric field, Energy Environ. Sci. 8 (2015) 995–1004. doi:10.1039/C4EE03664F.

[12] PVEducation, Electronics. http://www.pveducation.org/pvcdrom/characterisation/electronics (accessed September 18, 2017).

[13] D. Liu, T.L. Kelly, Perovskite solar cells with a planar heterojunction structure prepared using room-temperature solution processing techniques, Nat. Photonics. 8 (2013) 133–138. doi:10.1038/nphoton.2013.342.

[14] L.K. Ono, M.R. Leyden, S. Wang, Y. Qi, Organometal halide perovskite thin films and solar cells by vapor deposition, J. Mater. Chem. A. 4 (2016) 6693–6713. doi:10.1039/C5TA08963H.

[15] Y. Li, W. Yan, Y. Li, S. Wang, W. Wang, Z. Bian, L. Xiao, Q. Gong, Direct observation of long electron-hole diffusion distance in CH3NH3PbI3 Perovskite thin film, Sci. Rep. 5 (2015) 14485. doi:10.1038/srep14485.

[16] S.O. Kasap, Principles of electronic materials and devices, McGraw Hill Higher Education, New York.

[17] J. Nelson, Physics of Solar Cells, Imperial College Press, London, 2005.

[18] J. Takács, Mathematics of hysteretic phenomena: the T(x) model for the description of hysteresis, Wiley-VCH, Weinheim, 2003.

[19] K. Seki, Equivalent circuit representation of hysteresis in solar cells that considers interface charge accumulation: Potential cause of hysteresis in perovskite solar cells, Appl. Phys. Lett. 109 (2016) 3–7. doi:10.1063/1.4959247.

[20] M.A. Green, Solar cell fill factors: general graph and empirical expressions, Solid. State. Electron. 24 (1981) 788–789. doi:10.1016/0038-1101(81)90062-9.

[21] B. Chen, M. Yang, S. Priya, K. Zhu, Origin of J-V hysteresis in Perovskite solar cells., J. Phys. Chem. Lett. (2016). doi:10.1021/acs.jpclett.6b00215.

[22] Y. Wu, H. Shen, D. Walter, D. Jacobs, T. Duong, J. Peng, L. Jiang, Y.B. Cheng, K. Weber, On the origin of hysteresis in Perovskite solar cells, Adv. Funct. Mater. 26 (2016) 6807–6813. doi:10.1002/adfm.201602231.

[23] M. Grätzel, The light and shade of perovskite solar cells, Nat. Mater. 13 (2014) 838–842. doi:10.1038/nmat4065.

[24] C. Li, S. Tscheuschner, F. Paulus, P.E. Hopkinson, J. Kieβling, A. Köhler, Y. Vaynzof, S. Huettner, Iodine migration and its effect on hysteresis in Perovskite solar cells, Adv. Mater. 28 (2016) 2446–2454. doi:10.1002/adma.201503832.

[25] B. Chen, M. Yang, X. Zheng, C. Wu, W. Li, Y. Yan, J. Bisquert, G. Garcia-Belmonte, K. Zhu, S. Priya, Impact of Capacitive Effect and Ion Migration on the Hysteretic Behavior of Perovskite Solar Cells, J. Phys. Chem. Lett. 6 (2015) 4693–4700. doi:10.1021/acs.jpclett.5b02229.

[26] L.A. Frolova, N.N. Dremova, P.A. Troshin, The chemical origin of the p-type and n-type doping effects in the hybrid methylammonium–lead iodide (MAPbI3) Perovskite solar cells, Chem. Commun. 51 (2015) 14917–14920. doi:10.1039/C5CC05205J.

[27] H. Kim, C.M. Gilmore, A. Piqué, J.S. Horwitz, H. Mattoussi, H. Murata, Z.H. Kafafi, D.B. Chrisey, Electrical, optical, and structural properties of indium tin oxide thin films for organic light-emitting devices, J. Appl. Phys. 86 (1999) 6451–6461. doi:10.1063/1.371708.

[28] R. Bel Hadj Tahar, T. Ban, Y. Ohya, Y. Takahashi, Tin doped indium oxide thin films: electrical properties, J. Appl. Phys. 83 (1998) 2631–2645. doi:10.1063/1.367025.

[29] M. Thirumoorthi, J. Thomas Joseph Prakash, Structure, optical and electrical properties of indium tin oxide ultra thin films prepared by jet nebulizer spray pyrolysis technique, J. Asian Ceram. Soc. 4 (2016) 124–132. doi:10.1016/j.jascer.2016.01.001.

[30] B.J. Morgan, G.W. Watson, Intrinsic n-type defect formation in TiO2: a comparison of rutile and anatase from GGA + U calculations, J. Phys. Chem. C. 114 (2010) 2321–2328. doi:10.1021/jp9088047.

[31] A. Kitai, Principles of Solar Cells, LEDs and Diodes: The role of the PN junction, 2011.

[32] R.M. Hazen, Perovskites, Scientific American 258 (1988).

[33] V. Gonzalez-Pedro, E.J. Juarez-Perez, W.-S. Arsyad, E.M. Barea, F. Fabregat-Santiago, I. Mora-Sero, J. Bisquert, General working principles of CH3NH3PbX3 Perovskite solar cells, Nano Lett. 14 (2014) 888–893. doi:10.1021/nl404252e.

[34] Y.-C. Hsiao, T. Wu, M. Li, Q. Liu, W. Qin, B. Hu, Fundamental physics behind highefficiency organo-metal halide Perovskite solar cells, J. Mater. Chem. A. 0 (2015) 1–14. doi:10.1039/C5TA01376C.

[35] C. Eames, J.M. Frost, P.R.F. Barnes, B.C. O'Regan, A. Walsh, M.S. Islam, Ionic transport in hybrid lead iodide perovskite solar cells, Nat. Commun. 6 (2015) 7497. doi:10.1038/ncomms8497.

[36] J.H. Heo, S.H. Im, J.H. Noh, T.N. Mandal, C.-S. Lim, J.A. Chang, Y.H. Lee, H. Kim, A. Sarkar, M.K. Nazeeruddin, M. Grätzel, S. Il Seok, Efficient inorganic–organic hybrid heterojunction solar cells containing Perovskite compound and polymeric hole conductors, Nat. Photonics. 7 (2013) 486–491. doi:10.1038/nphoton.2013.80.

[37] C.-S. Jiang, M. Yang, Y. Zhou, B. To, S.U. Nanayakkara, J.M. Luther, W. Zhou, J.J. Berry, J. van de Lagemaat, N.P. Padture, K. Zhu, M.M. Al-Jassim, Carrier separation and transport in Perovskite solar cells studied by nanometre-scale profiling of electrical potential, Nat. Commun. 6 (2015) 8397. doi:10.1038/ncomms9397.

[38] J.H. Heo, S.H. Im, CH3NH3PbI3/poly-3-hexylthiophene Perovskite mesoscopic solar cells: performance enhancement by Li-assisted hole conduction, Phys. Status Solidi - Rapid Res. Lett. 8 (2014) 816–821. doi:10.1002/pssr.201409330.

[39] J. Yang, K.M. Fransishyn, T.L. Kelly, Comparing the effect of mesoporous and planar metal oxides on the stability of methylammonium lead iodide thin films, Chem. Mater. 28 (2016) 7344–7352. doi:10.1021/acs.chemmater.6b02744.

[40] T. Leijtens, T. Giovenzana, S.N. Habisreutinger, J.S. Tinkham, N.K. Noel, B.A. Kamino, G. Sadoughi, A. Sellinger, H.J. Snaith, Hydrophobic organic hole transporters for improved moisture resistance in metal halide Perovskite solar cells, ACS Appl. Mater. Interfaces. 8 (2016) 5981–5989. doi:10.1021/acsami.5b10093.

[41] Ossila, Spin Coating: A Guide to Theory and Techniques. https://www.ossila.com/pages/spincoating (accessed October 17, 2017).

[42] G.M. Alonzo-Medina, a González-González, J.L. Sacedón, a I. Oliva, Understanding the thermal annealing process on metallic thin films, IOP Conf. Ser. Mater. Sci. Eng. 45 (2013) 12013. doi:10.1088/1757-899X/45/1/012013.

[43] G. Dong, Y. Yang, L. Sheng, D. Xia, T. Su, R. Fan, Y. Shi, J. Wang, Inverted thermal annealing of Perovskite films: a method for enhancing photovoltaic device efficiency, RSC Adv. 6 (2016) 44034–44040. doi:10.1039/C6RA07497A.

[44] E.E. Schneider, The electronic structure of solids, Sci. Prog. 36 (1948) 614–632. doi:10.1002/9783527646463.ch1.

[45] A. Rockett, The materials science of semiconductors, Springer, New York, 2008.

[46] K. Tvingstedt, O. Malinkiewicz, A. Baumann, C. Deibel, H.J. Snaith, V. Dyakonov, H.J. Bolink, Radiative efficiency of lead iodide based Perovskite solar cells, Sci. Rep. 4 (2015) 6071. doi:10.1038/srep06071.

[47] A. Asadpoordarvish, A. Sandström, S. Tang, J. Granström, L. Edman, Encapsulating lightemitting electrochemical cells for improved performance, Appl. Phys. Lett. 100 (2012) 193508. doi:10.1063/1.4714696.

[48] J.-W. Lee, D.-H. Kim, H.-S. Kim, S.-W. Seo, S.M. Cho, N.-G. Park, Formamidinium and cesium hybridization for photo and moisture stable Perovskite solar cell, Adv. Energy Mater. 5 (2015) 1501310. doi:10.1002/aenm.201501310.

[49] J.-H. Im, I.-H. Jang, N. Pellet, M. Grätzel, N.-G. Park, Growth of $CH_3NH_3PbI_3$ cuboids with controlled size for high-efficiency Perovskite solar cells., Nat. Nanotechnol. 9 (2014) 927–932. doi:10.1038/nnano.2014.181.

[50] J. Yang, K.M. Fransishyn, T.L. Kelly, Comparing the effect of mesoporous and planar metal oxides on the stability of methylammonium lead iodide thin films, Chem. Mater. 28 (2016) 7344–7352. doi:10.1021/acs.chemmater.6b02744.

[51] L.L. Bu, Z.H. Liu, M. Zhang, W.H. Li, A.L. Zhu, F.S. Cai, Z.X. Zhao, Y.H. Zhou, Semitransparent fully air processed Perovskite solar cells, ACS Appl Mater Interfaces. 7 (2015) 17776–17781. doi:10.1021/acsami.5b04040.

[52] J.-H. Im, I.-H. Jang, N. Pellet, M. Grätzel, N.-G. Park, Growth of CH3NH3PbI3 cuboids with controlled size for high-efficiency Perovskite solar cells., Nat. Nanotechnol. 9 (2014) 927–932. doi:10.1038/nnano.2014.181.

[53] J.H. Heo, H.J. Han, D. Kim, T.K. Ahn, S.H. Im, Hysteresis-less inverted CH3NH3PbI3 planar Perovskite hybrid solar cells with 18.1% power conversion efficiency, Energy Environ. Sci. 8 (2015) 1602–1608. doi:10.1039/C5EE00120J.

[54] G. Ma, H.C. Allen, Handbook of spectroscopy, Wiley-VCH Verlag GmbH & Co. KGaA,Weinheim, 2003.

[55] Y. Yu, J. Li, D. Geng, J. Wang, L. Zhang, T.L. Andrew, M.S. Arnold, X. Wang, Development of lead iodide Perovskite solar cells using three-dimensional titanium dioxide nanowire architectures., ACS Nano. 9 (2015) 564–572. doi:10.1021/nn5058672.

[56] M. Liu, M.B. Johnston, H.J. Snaith, Efficient planar heterojunction Perovskite solar cells by vapour deposition, Nature. 501 (2013) 395–398. doi:10.1038/nature12509.

[57] Q. Tai, P. You, H. Sang, Z. Liu, C. Hu, L.W. Helen, Efficient and stable Perovskite solar cells prepared in ambient air irrespective of the humidity, Nat. Commun. 6 (2016) 1–8. doi:10.1038/ncomms11105.

[58] E. Ugur, A.D. Sheikh, R. Munir, J.I. Khan, D. Barrit, A. Amassian, F. Laquai, Improved morphology and efficiency of n−i−p Planar Perovskite solar cells by processing with glycol ether additives, (2017). doi:10.1021/acsenergylett.7b00526.

[59] M. Yang, Y. Zhou, Y. Zeng, C. Jiang, N.P. Padture, K. Zhu, Square-centimeter solution-processed planar CH3NH3PbI3 Perovskite solar cells with efficiency exceeding 15%, (2015)

6363–6370. doi:10.1002/adma.201502586.

[60] Q. Chen, H. Zhou, Z. Hong, S. Luo, H. Duan, H. Wang, Y. Liu, G. Li, Y. Yang, Planar heterojunction Perovskite solar cells via vapor-assisted solution process, (2014) 3–6. doi:10.1021/ja411509g.

[61] S. Agarwal, P.R. Nair, Pinhole induced efficiency variation in Perovskite solar cells, J. Appl. Phys. J. Appl. Phys. J. Appl. Phys. Appl. Phys. Lett. Appl. Phys. Rev. Junction Sol. Cells J. Appl. Phys. J. Appl. Phys. 1221 (2017) 163104–143901. doi:10.1063/1.1736034.

[62] J.J. Choi, X. Yang, Z.M. Norman, S.J.L. Billinge, J.S. Owen, Structure of methylammonium lead Iodide within mesoporous titanium dioxide: active material in high-performance Perovskite solar cells, (2013). doi:10.1021/nl403514x.

[63] N.J. Jeon, J.H. Noh, W.S. Yang, Y.C. Kim, S. Ryu, J. Seo, S. Il Seok, Compositional engineering of Perovskite materials for high-performance solar cells, Nature. 517 (2015) 476–480. doi:10.1038/nature14133.

[64] J.H. Heo, H.J. Han, D. Kim, T.K. Ahn, S.H. Im, Hysteresis-less inverted CH3NH3PbI3 planar Perovskite hybrid solar cells with 18.1% power conversion efficiency, Energy Environ. Sci. 8 (2015) 1602–1608. doi:10.1039/C5EE00120J.

[65] Y. Xiao, G. Han, Y. Chang, Y. Zhang, Y. Li, M. Li, Investigation of Perovskite-sensitized nanoporous titanium dioxide photoanodes with different thicknesses in Perovskite solar cells, J. Power Sources. 286 (2015) 118–123. doi:10.1016/j.jpowsour.2015.03.152.

[66] T.C. Sum, The Photophysics of perovskite solar cells, (2014) 91650Y. doi:10.1117/12.2060297.

[67] P.A. Lane, Z.H. Kafafi, Solid-state organic photovoltaics: a review of molecular and polymeric devices, in: S. Sun, N.S. Sariciftci (Eds.), Organic photovoltaics: mechanisms, materials, and devices, Taylor & Francis, Florida, 2005.

[68] Adrian Kitai, Organic Semiconductors, OLEDs and Solar Cells, 2011 doi:10.1002/9781119974543.ch6.

[69] N.G. Park, Perovskite solar cells: An emerging photovoltaic technology, Mater. Today. 18 (2015) 65–72. doi:10.1016/j.mattod.2014.07.007.

[70] C. Chueh, C. Li, A.K. Jen, Recent progress and perspective in solution-processed interfacial

materials for effi cient and stable polymer and organometal Perovskite solar cells, Energy Environ. Sci. 18 (2015) 1160–1189. doi:10.1039/C4EE03824J.

[71] J. Burschka, N. Pellet, S.-J. Moon, R. Humphry-Baker, P. Gao, M.K. Nazeeruddin, M Grätzel, Sequential deposition as a route to high-performance Perovskite-sensitized solar cells., Nature. 499 (2013) 316–320. doi:10.1038/nature12340.

[72] J. Cui, H. Yuan, J. Li, X. Xu, Y. Shen, H. Lin, M. Wang, Recent progress in efficient hybrid lead halide Perovskite solar cells, Sci. Technol. Adv. Mater. 16 (2015) 36004. doi:10.1088/1468-6996/16/3/036004.

[73] G. Hu, W. Guo, R. Yu, X. Yang, R. Zhou, C. Pan, Z.L. Wang, Enhanced performances of flexible ZnO/Perovskite solar cells by piezo-phototronic effect, Nano Energy. 23 (2016) 27–33. doi:10.1016/j.nanoen.2016.02.057.

[74] Y. Fu, F. Meng, M.B. Rowley, B.J. Thompson, M.J. Shearer, D. Ma, R.J. Hamers, J.C. Wright, S. Jin, Solution growth of single crystal methylammonium lead halide Perovskite nanostructures for optoelectronic and photovoltaic applications, J. Am. Chem. Soc. 137 (2015) 5810–5818. doi:10.1021/jacs.5b02651.

[75] J. Yang, B.D. Siempelkamp, D. Liu, T.L. Kelly, Investigation of CH3NH3PbI3 degradation rates and mechanisms in controlled humidity environments using in situ techniques, ACS Nano. 9 (2015) 1955–1963. doi:10.1021/nn506864k.

[76] N. Aristidou, I. Sanchez-Molina, T. Chotchuangchutchaval, M. Brown, L. Martinez, T. Rath, S.A. Haque, The role of oxygen in the degradation of methylammonium lead trihalide Perovskite photoactive layers, Angew. Chemie-Int. Ed. 54 (2015) 8208–8212. doi:10.1002/anie.201503153.

[77] A.M.A. Leguy, Y. Hu, M. Campoy-Quiles, M.I. Alonso, O.J. Weber, P. Azarhoosh, M. van Schilfgaarde, M.T. Weller, T. Bein, J. Nelson, P. Docampo, P.R.F. Barnes, Reversible hydration of CH3NH3PbI3 in films, single crystals, and solar cells, Chem. Mater. 27 (2015) 3397–3407. doi:10.1021/acs.chemmater.5b00660.

[78] J.C. Pramudita, R. Aughterson, W.M. Dose, S.W. Donne, H.E.A. Brand, N. Sharma, Using in situ synchrotron x-ray diffraction to study lithium- and sodium-ion batteries: a case study with an unconventional battery electrode (Gd2TiO5), J. Mater. Res. 30 (2015) 381–389.

doi:10.1557/jmr.2014.311.

[79] A. Mecherikunnel, J. Richmond, Spectral distribution of solar radiation, NASA STI/Recon Tech. (1980). doi:10.1002/qj.49710444112.

[80] Solar Spectral Irradiance: Air Mass 1.5. http://rredc.nrel.gov/solar/spectra/am1.5/ (accessed December 13, 2017).

[81] S.J. Byrnes, The Shockley-Queisser limit. http://sjbyrnes.com/sq.html (accessed December 13, 2017).

[82] M.Z. Jacobson, M.A. Delucchi, Providing all global energy with wind, water, and solar power, Part I: technologies, energy resources, quantities and areas of infrastructure, and materials, Energy Policy. 39 (2011) 1154–1169. doi:10.1016/j.enpol.2010.11.040.

[83] C.H. Henry, Limiting efficiencies of ideal single and multiple energy gap terrestrial solar cells, J. Appl. Phys. 51 (1980) 4494–4500. doi:10.1063/1.328272.

[84] National Renewable Energy Laboratory, National Renewable Energy Laboratory (NREL) research cell record efficiency chart. https://www.nrel.gov/pv/assets/images/efficiencychart. png (accessed August 6, 2017).

APPENDIX A

The Solar Resource

Solar Power Available Before Attenuation

The sun's spectrum can be modelled as that of a 5760 K black body. The radiation power density of the sun on its surface can then be calculated using the Stefan-Boltzmann law as seen in Equation A.1.

$$P_{Ssurface} = \sigma T^4 = (5.67 \times 10^{-8} W m^{-2} K^{-4})(5760\ K)^4 = 62 MW/\mathrm{m}^2 \quad \text{(A.1)}$$

where $P_{Ssurface}$ represents the power of the sun at its surface, σ is the Stefan-Boltzmann constant, and T represents the temperature of the sun. The solar radiation power density, or irradiance, on the sun's surface is 62 MW/m^2. However, if one considers an area just outside the earth's atmosphere this value is 1353 W/m^2 [17]. This reduction is due to the reduced angular range of the sun. The earth's position is such that it is out of the range of a large portion of the radiation being emitted from the sun. The earth is 1.5×10^{11} m away from the sun. This means that at this distance (R_{earth}), the area irradiated by the sun (A_{rad}) is given by Equation A.2.

$$A_{rad} = 4\pi R_{earth}^2 = 2.83 \times 10^{23}\ \mathrm{m}^2 \quad \text{(A.2)}$$

Consider that the total power output from the sun (P_{Tot}) is given by,

$$P_{Tot} = 62\ \mathrm{MW/m}^2 \times A_{Sun} = (62\ \mathrm{MW/m}^2 \times 6.16 \times 10^{18}\ \mathrm{m}^2) \quad \text{(A.3)}$$

$$= 3.9 \times 10^{26}\ \mathrm{W}$$

where A_{Sun} is the surface area of the sun. It then follows, that the radiation at a point just outside of the earth's atmosphere should be,

$$Rad_{eart} = \frac{P_{Tot}}{A_{rad}} = 1353\ \mathrm{W}/m^2 \quad \text{(A.4)}$$

where Rad_{earth} is the radiation at a point just outside of the earth's atmosphere. This marks a reduction by a factor of 4.58×10^4, when comparing the irradiance values at the surface of the sun to those just outside of earth's atmosphere. Since the sun's spectral intensity can be modelled as that of a 5760 K black body [17], it is therefore reasonable to model the spectrum of the sun just outside of the earth's atmosphere as that of a 5760 K black body, but reduced by a factor of 4.58×10^4. It should be noted however that after this solar radiation passes through the earth's atmosphere, it is attenuated by components of the atmosphere such as the various constituent gases, aerosols and dust particles [79]. To more accurately model the solar spectrum after attenuation, the Air Mass (AM) 1.5 standard was defined.

Power Available After Attenuation

AM refers to the thickness of atmosphere that sunlight must pass through and is calculated using Equation A.5. How this value is calculated is illustrated in Figure A.1 where γ is the elevation angle of the sun.

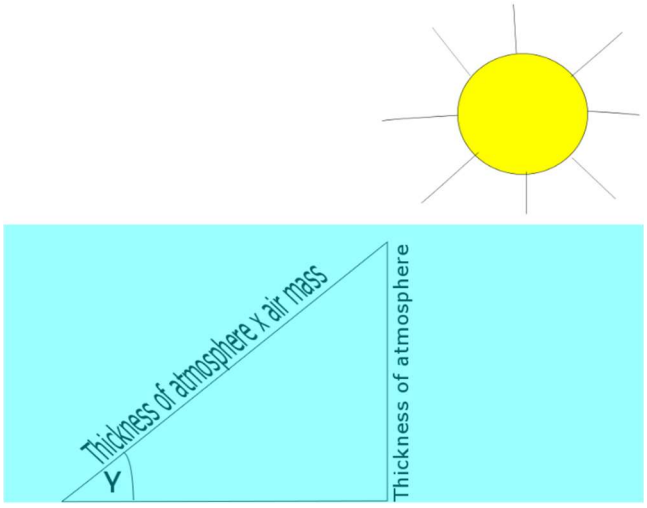

Figure A.1. An illustration of the concept of air mass. At elevation angle γ, light from the sun must travel through an increased optical path of (thickness of atmosphere × air mass).

$$Air\ mass = \frac{actual\ optical\ path}{thickness\ of\ atmosphere} = \text{cosec}\,\gamma \tag{A.5}$$

The AM 1.5 spectrum is the spectrum of the sun at a point just outside of the earth's atmosphere, attenuated by 1.5 thicknesses of the atmosphere [17]. This gives a value for irradiance of about 900 W/m^2 [17]. However, the irradiance of the AM 1.5 spectrum is normalized to 1000 W/m^2 for simplicity. The quantity of 1000 W/m^2 is commonly referred to as one sun illumination [17]. Light with a wavelength of less than 300 nm is mostly blocked by atomic and molecular oxygen as well as by ozone and nitrogen (N_2). In the infrared region, water and CO_2 are responsible for the attenuation observed [17]. Their effects on the power available from different wavelengths of light from the sun are illustrated in Figure A.2. This graph was plotted using data from the National Renewable Energy Laboratory of the U.S [80]. Steven Byrne's adapted Python™ code [81] was used to make the plot.

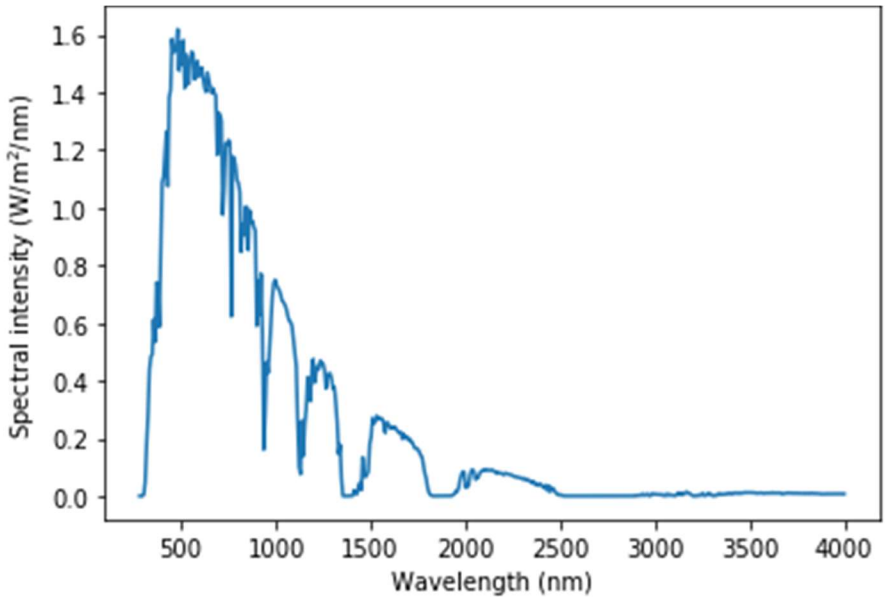

Figure A.2. AM 1.5 solar spectrum. The dips represent absorption due to O_2, O_3, N_2, H_2O and CO_2.

Total Power Delivered to Earth's Surface versus Global Power Demand

Considering that the earth has a cross-sectional area (A_{xearth}) of 1.3×10^{14} m^2, the power (P_{iear}) delivered from the sun to the illuminated portion of the earth at an instant, can be given by Equation A.6.

$$P_{iear} = \frac{1000\ \mathrm{W}}{\mathrm{m}^2} \times (1.3 \times 10^{14}\ \mathrm{m}^2) = 1.30 \times 10^{17}\ \mathrm{W} \tag{A.6}$$

Global power demand is currently estimated to be 1.25×10^{13} W [82]. The power delivered to the earth outstrips this demand by 4 orders of magnitude. P_{iear} will of course vary as the solar intensity will not be constant. Factors such as changes in the power output from the sun, varying weather conditions and solar converter efficiency, must be taken into consideration. However, Equations A.4 – A.6, at the very least, demonstrate that PV solar cells are a method of energy generation that are worth investigating.

Detailed Balance: The Ultimate Efficiency for an Ideal Photovoltaic Solar Cell Operating on Earth (AM 1.5 Spectrum)

Photon Flux

Consider that the power density per unit wavelength of the sun is given by

$$P_{sden} = \frac{8\pi hc^2}{\lambda^5} \frac{1}{e^{hc/\lambda kT_s} - 1} \tag{A.7}$$

where P_{sden} is the power density per unit wavelength of the sun in W/m^3, λ is the wavelength of emitted radiation, h is planck's constant, T_s is the temperature of the sun, c is the speed of light, and k is Boltzmann's constant. Considering that the photon flux emitted (Φ_S) from the sun is

$$\Phi_S = \frac{P_{sden} \times \lambda}{hc} \tag{A.8}$$

It then follows that the photon flux can be represented by Equation A.9 [17].

$$\Phi_S = \frac{2F_s}{h^3c^2} \left(\frac{E^2}{e^{E/kT_s} - 1}\right) \tag{A.9}$$

In Equation A.9, Φ_S is given in photons/m^2/s/J. E represents the corresponding photon energy ($E = hc/\lambda$). F_s is a geometrical factor which arises due to the curvature of the sun. At the surface of

the sun, its value is simply π. We showed earlier that at a point just outside earth's atmosphere, the power emitted by the sun is reduced by a factor of 4.58×10^4. It is reasonable to also use this value when making considerations on the earth surface. F_s on the surface of the earth must also be reduced by this factor. This gives a value of $F_s = 2.18 \times 10^{-5}$ on earth's surface.

Solar Cell under Illumination

We must now consider a PV solar cell under illumination. Before beginning, it should be noted that both the solar cell and its surroundings emit long-wavelength thermal photons. The thermal emission of the solar cell must be balanced by its absorption to ensure that the electron concentration at a steady state remains constant [17]. When a solar cell absorbs solar energy, a portion of the electron population within the device is raised to an electrochemical potential $\Delta\mu$. Equation A.9 is modified as follows to quantify emission of photons from the solar cell:

$$\Phi_e(E, \Delta\mu) = F_e \frac{2n_s^2}{h^3c^2} \frac{E^2}{e^{(E-\Delta\mu)/kT_a} - 1} \quad \text{(A.10)}$$

where F_e is the geometrical factor which takes into consideration the angular range of photon emission from the solar cell and is given by

$$F_e = \pi sin^2\theta_c = \pi \frac{n_0^2}{n_s^2} \quad , \quad \text{(A.11)}$$

where n_0 is the refractive index of air and n_s is the refractive index of the solar cell and,

$$\theta_c = sin^{-1}(\frac{n_0}{n_s}) \quad . \quad \text{(A.12)}$$

Equation A.12 results from Snell's law. On a surface with air, $n_s = 1$. This means that for a surface with air,

$$F_e \times n_s^2 = F_a = 1 \quad . \quad \text{(A.13)}$$

where F_a is the geometrical factor taking the range of absorption of the solar cell into consideration. Thus Equation A.10 becomes

$$\Phi_e(E, \Delta\mu) = \frac{2F_a}{h^3c^2}\frac{E^2}{e^{(E-\Delta\mu)/kT_a} - 1} \quad . \quad \text{(A.14)}$$

The photon emission current density can then be written as

$$J_{rad}(E) = q(1 - R(E))\varepsilon(E)\Phi_e(E, \Delta\mu) \quad . \quad \text{(A.15)}$$

Equation A.15 assumes that for each photon absorbed, there is an electron generated. The emissivity of the solar cell, ε(E), is the probability that the cell will emit a photon. *R(E)* is the probability of an emitted photon being reflected. This emission occurs due to the temperature of the cell, T_C, which is assumed in this example to be equal to T_a. Planck's radiation law dictates that a body with temperature *T*, absorbing photons, must conversely emit photons. This loss is an unavoidable loss in a solar cell unless the device is maintained at 0 K.

Now, we must take photon absorption into consideration. The flux of photons emitted from the ambient environment as well as solar photons is given by

$$\Phi_a(E) = \frac{2F_a}{h^3c^2}\left(\frac{E^2}{e^{E/kT_s} - 1}\right) \quad , \quad \text{(A.16)}$$

In the case of F_a is π, assuming that absorption occurs over a hemisphere. The current density corresponding to photon absorption can then be written as

$$J_{abs}(E) = q\big(1 - R(E)\big)a(E)\left[\Phi_s(E) + \left(1 - \frac{F_s}{F_a}\right)\Phi_a(E)\right] \quad \text{(A.17)}$$

where *a(E)* is the probability of a photon being absorbed. The net equivalent current density (J_{net}) is then given by,

$$J_{net} = J_{abs}(E) - J_{rad}(E) \quad . \quad \text{(A.18)}$$

J_{net} can be divided into the contributions from absorption and emission. For net absorption, we have

$$J_{abs(net)} = q\big(1 - R(E)\big)a(E)\left[b_s(E) - \frac{F_s}{F_a}\Phi_a(E)\right] \quad . \quad \text{(A.19)}$$

For a net emission, which is also known as the radiative recombination current density, we have

$$J_{rad(net)} = q\big(1 - R(E)\big)a(E)[\Phi_e(E, \Delta\mu) - \Phi_e(E, 0)] \quad . \quad \text{(A.20)}$$

where $\Phi_e(E,0) = \Phi_a(E)$. It should be noted that radiative recombination is an intrinsic loss which cannot be avoided [83].

Highest Possible Efficiency for a Solar Cell Under AM 1.5 Solar Spectrum

This explanation will make use of a 2-band semiconductor model. These 2 bands are separated by a bandgap (E_g). Photons with energy less than the bandgap will not contribute to the current output of a photovoltaic solar cell. The photocurrent produced by a solar cell results from the net solar photon flux absorbed as given by Equation A.17. The last term, $(1 - \frac{F_s}{F_a})\Phi_a(E)$, in the equation can be neglected since it is small compared to the $\Phi_s(E)$ term. Assuming that each electron has a probability η_{Col} of being collected and transported to an external circuit to do useful work, we can represent the short-circuit current density (J_{SC}) as

$$J_{SC} = q\int_0^\infty \eta_{col}(E)\big(1 - R(E)\big)a(E)\Phi_s(E)dE \quad . \quad \text{(A.21)}$$

Furthermore, we assume that all incident photons are absorbed and each photon produces only one electron. We also assume that all of the photo generated electrons are collected. Equation A.21 then reduces to

$$J_{SC} = q\int_{E_g}^\infty \Phi_s(E)dE \quad \text{(A.22)}$$

where E_g is the bandgap energy, and J_{SC} is now just a function of the incident solar spectrum and the energy bandgap of our solar cell.

We will only consider losses due to radiative recombination in an ideal case. The dark current (J_{dark}) density due to this process is

$$J_{dark}(V) = J_{rad}(\Delta\mu) \quad \text{(A.23)}$$

$$= q \int \big(1 - R(E)\big) a(E) [\Phi_e(E, \Delta\mu) - \Phi_e(E, 0)] dE$$

Finally, the net current can be given by,

$$J_{net}(V) = J_{SC} - J_{dark}(V) \tag{A.24}$$

$$= q \int_0^\infty \big(1 - R(E)\big) a(E) \{\Phi_s(E) - [b_e(E, \Delta\mu) - b_e(E, 0)]\} dE$$

For the case where a photon must have energy $E \geq E_g$ and only one photon is generated, this reduces to Equation A.25.

$$J_{net}(V) = q \int_{E_g}^\infty \{\Phi_s(E) - [\Phi_e(E, qV) - \Phi_e(E, 0)]\} dE \tag{A.25}$$

Due to the bias dependence on the exponential term in Equation A.10, we can represent Equation A.25 as

$$J_{net}(V) = J_{SC} - J_0(e^{\frac{qV}{kT}} - 1) \quad . \tag{A.26}$$

The applied bias to a solar cell is at a maximum when the 2 terms in Equation A.26 cancel out meaning that $J_{net}(V) = 0$. This gives the open-circuit voltage (V_{OC}),

$$V_{OC} = \frac{kT}{q} ln(\frac{J_{SC}}{J_0} + 1) \quad . \tag{A.27}$$

Now, consider the incident power density of the sun, this is given by Equation A.28.

$$P_{sun} = \int_0^\infty E \Phi_s(E_s) dE \tag{A.28}$$

The power output of the solar cell is given by

$$P_{scell} = V \times J(V) \quad . \tag{A.29}$$

This means that the efficiency of a solar cell can be given by the following,

$$\eta = \frac{P_{scell}}{P_{sun}} \quad . \qquad \text{(A.30)}$$

The maximum efficiency for a given bandgap occurs when

$$\frac{d}{dV}[V \times J(V)] = 0 \qquad \text{(A.31)}$$

The corresponding values of V and $J(V)$ are V_{MPP} and J_{MPP}. These values are the maximum power point (MPP) values of voltage and current respectively. Figure A.3 illustrates the results obtained from a numerical method of determining the maximum possible efficiency for a solar cell operating in the conditions set out. Steven Byrne's adapted Python™ code [81] was used to make the plot. The maximum efficiencies for various bandgaps are calculated based on Equation A.30. The value for P_{scell} corresponds to V_{MPP} and J_{MPP} for a given bandgap.

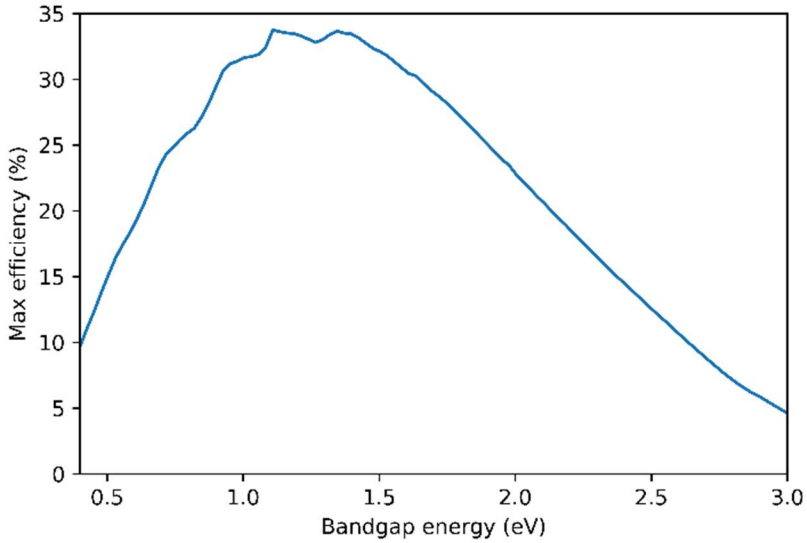

Figure A.3. A graphical representation of the maximum efficiencies possible for an ideal solar cell operating in the AM 1.5 spectrum.

These values are 'computed' numerically using Python™ code. V_{MPP} and J_{MPP}, correspond to a maximum power point value (P_{scell}), where V_{MPP} lies between 0 and $V_{OC,}$ and J_{MPP} lies between J_{SC} and 0. This makes P_{scell} for a given bandgap simple to determine numerically, given Equations A.1 – A.31. It is found that the maximum possible value for a solar cell operating in the AM 1.5

spectrum occurs around 1.4 eV and is about 33% [17,83]. The maximum possible efficiency for a $CH_3NH_3PbI_3$ PSC with a 1.5 eV bandgap is around 31% from Figure A.3.

Harnessing The Energy of The Sun With A Non-Ideal Solar Cell

It should be reiterated that several assumptions made are as follows [17]:

- The material responsible for photovoltaic action consists of discrete states which are either full or empty normally
- All photons with energy greater than the bandgap are absorbed
- Each absorbed photon creates an electron-hole pair (EHP)
- Radiative recombination is the only type of recombination occurring
- Generated EHPs are completely separated and losslessly extracted to an external circuit.

Taking these assumptions into consideration, the efficiency of an ideal 2-band solar cell is dependent only on the incident spectrum, and the bandgap of the solar cell. We are considering the AM 1.5 spectrum. This means that the efficiency of a solar cell meeting the conditions set out in this formulation depends only on its bandgap. The losses that are considered to make the plot for Figure A.3 are as follows:

- Photon energy above the bandgap of a solar cell is wasted. Photons with energy above the bandgap gives the same result (1 EHP) as photons whose energy match the bandgap.
- Below bandgap photons pass straight through the solar cell.
- There are losses due to unavoidable radiative recombination
- The voltage at the MPP is less than the bandgap voltage.

Figure A.4 highlights these losses. Steven Byrne's adapted Python™ code [16] was used to make the plot. Real-world, non-ideal solar cell do not function eactly as outlined.

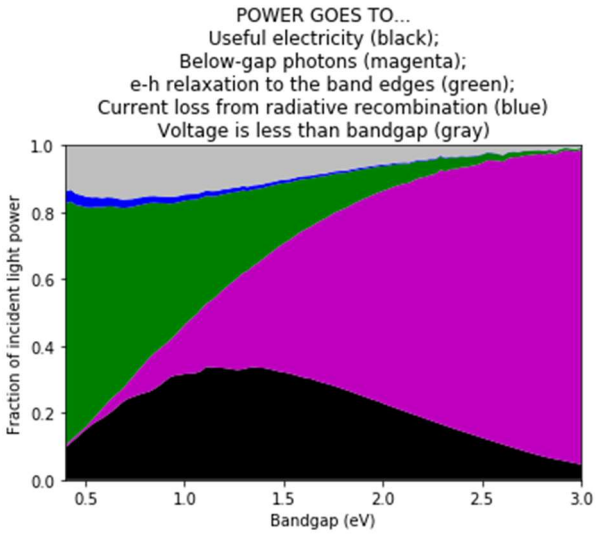

Figure A.4: The useful and wasted power in the case of the ideal solar cell considered in Section 2.2.3 (adapted from Steven Byrne's Python™ code [16]).

The following factors must be taken into consideration with a non ideal solar cell [17]:

- All of the light falling on the solar cell will not be absorbed.
- There will be parasitic resistances which will limit the device power output.
- Other types of recombination besides radiative recombination will occur.

These factors result in single band gap devices which possess PCEs less than the theoretical maximum in the AM 1.5 spectrum of 33 %. There are however, a few technologies which have surpassed a PCE of 20 %. Crystalline silicon (Si), crystalline gallium arsenide (GaAs), thin-film Si, thin-film copper indium gallium selenide (CuInGaSe) and thin-film cadmium telluride (CdTe) are well established solar cell architectures which have exceeded this mark [84]. Recently PSCs have also exceeded the 20 % mark [7].

APPENDIX B

Figure Reproduction Permissions

- Figure 5.5 Reproduced (adapted) from Ref. 11 with permission from the Royal Society of Chemistry.
- Figure 2.17 Reproduced (adapted) from Ref. 21 with permission of the publisher of J. Phys. Chem. Lett.

.